Master's Degree Thesis

Silicon nanoantenna designs for optical-frequency electronics

Supervisors

Dr. Phillip KEATHLEY
Prof. Renato GONNELLI

Candidate

Marco RAFFA

Master's Degree in Micro- and Nanotechnologies for Integrated Systems

POLITECNICO DI TORINO, GRENOBLE-INP, EPFL

October 2023

Acknowledgement

I would like to express my sincere gratitude to Dr. Phillip Keathley and Prof. Renato Gonnelli for their invaluable guidance, unwavering support, and expert advice throughout the course of this research. Their mentorship was instrumental in shaping the direction of this thesis.

I am also thankful to Matthew Yeung and Prof. Marco Colangelo for their insightful feedback and constructive criticism, which greatly improved the quality of this work.

I extend my appreciation to Prof. Karl Berggren and the entire Quantum Nanostructures and Nanofabrication (QNN) Group at MIT. Thank you for believing in me and for welcoming me to this outstanding university.

I must also mention my two friends, Francesca and Marco. Thank you for the incredible journey in the USA; without you, this experience would not have been as successful and memorable.

I am indebted to my family for their financial support, which allowed me to stay in the Boston area, and for their unconditional confidence in my abilities. I hope to repay your trust in the future.

Lastly, I want to acknowledge the unwavering support of two colleagues from the Nanotech program.

Roberta, thank you for being a source of strength through all the challenges we faced in these two years. Even if it wasn't often explicitly said, I am grateful to have shared this university experience with you.

Elisa, we spent almost the entire master's degree experience together. We've been through good and bad times, and I couldn't be happier to have met you. I am grateful for each other's help in overcoming problems, for the encouragement before each exam, and for the dinners you prepared for me. I am hopeful that our paths will cross again in the future.

This research would not have been possible without the collective support and encouragement of all those mentioned above. Thank you for believing in me and helping me reach this milestone.

Marco Raffa

Contents

1 Introduction

Electron photoemission is a physical phenomenon related to the interaction between light and matter. When an electromagnetic wave impinges on a material, it can transfer its energy to one of the electrons bound within the target. If this energy is equal to or greater than the binding energy of the electron, it can be emitted from the material and contribute to a finite electrical current.

Considering light as a set of discrete energy packets called photons, the photoemission process is said to be linear if the energy of only one photon is transferred to emit the electron. If more than one photon is involved in the energy transfer process, the electron photoemission is said to be non-linear.

In the non-linear regime, if the optical field is strong enough to bend the energy barrier between the material and the vacuum and to let the electron tunnel out, it is possible to generate sub-optical-cycle current pulses that are synchronized with the optical field waveform. Therefore, the photoemitted current will be dependent on the phase of the impinging pulse.

This particular regime is called optical-field-driven tunneling emission and, thanks to the sub-optical-cycle temporal resolution of the current pulses, it has technological applications like time-domain field sampling [1], petahertz (PHz) optoelectronics [2], and carrier-envelope-phase (CEP) detection [3].
In order to bend the energy barrier and observe electron tunneling, large electric fields are required. However, the field strength necessary to enter the optical-field-driven tunneling emission regime is often above the damage threshold of the device. The amount of energy is too high to be efficiently dissipated by the device, the thermal load rapidly grows and the device reaches temperature that causes degradation of the target. The use of an ultra-short pulsed laser becomes interesting in this case: high electric field peaks shine on the device just for a really short time, keeping the average power in a pulse period below the damage threshold. Moreover, some field enhancement (FE) mechanisms are investigated to observe the non-linear physics in light-matter interaction. FE is defined as the ratio between the local electric field and the incident one; it can be exploited in light interaction with nanostructures through plasmonic or similar resonance mechanisms. In this work, the combination of these two mechanisms (pulsed laser and FE) is explored to access optical-field-driven tunneling emission regimes for planar devices and to overcome actual device limitations. Plasmonic devices based on gold can reach high FE but they suffer from degradation after irradiation [3], a more robust plasmonic material like TiN can, instead, sustain high electric field but it does not achieve optical tunneling reliably [4].

Nanoantennas provide an attractive means to obtain a local electric field above the optical-field-driven tunneling threshold in confined regions of space and time, thereby avoiding device damage. Nanoantennas are investigated in the non-linear regime due to their high degree of freedom in geometric design and in materials choice; these characteristics, together with a well-established fabrication process, permit the realization of on-chip devices able to exploit the optical field-driven tunneling emission.

The main objective of this master's thesis is to investigate new geometrical designs and materials for nanoantennas in order to explore new physics behaviors and resonance mechanisms. In a previous work based on nanostructured silicon-tip array [5], an optical-field-driven tunneling emission regime has been demonstrated thanks to the material strength and the possibility to achieve FE even without plasmonic-based resonances. These two qualities make the silicon a good candidate to realize planar array devices able to exploit optical-field-driven tunneling.

Through this work, I studied and designed planar silicon nanoantennas that rely on Fabry-

Perot-like resonance. The magnitude of the FE achieved in silicon nanostructures is similar to the one achieved in gold devices, therefore the capability of planar silicon nanoantennas to detect the phase of the incident pulses is also investigated.

The research begins by starting with finite element method (FEM) simulations in chapter 6. Different shapes and layouts will be simulated to evaluate the intensity of the field enhancement in the near-infrared and visible regions for silicon-based nanoantennas.

The simulated data are then analyzed using suitable MATLAB® codes to evaluate the expected device performance: CEP sensitivity and signal-to-noise ratio (SNR). These quantities are compared, in chapter 7, for different designs and different incident pulses, to check for which combination yields the best performance.

In the last part of this master's thesis, chapter 8, multiple array devices are fabricated in a cleanroom facility to evaluate the feasibility of the geometry proposed in the design/simulation phase and to check the possibility of exploiting the optical-field-driven tunneling mechanism in silicon.

2 Electron photoemission regimes

2.1 Linear photoemission

Electron photoemission is a physical mechanism of light-matter interaction. When electromagnetic radiation strikes a metallic material with sufficient energy to overcome the potential barrier between the electron energy level (Fermi level, E_F) and the vacuum level ($-e\Phi$, which is the rest energy of the electron in vacuum), electrons are ejected [Fig.1]. If the binding energy (work function, $W_F = -e\Phi - E_F$) is transferred from a single photon with energy $h\nu \geq W_F$, the emission phenomenon scales linearly with the optical intensity.

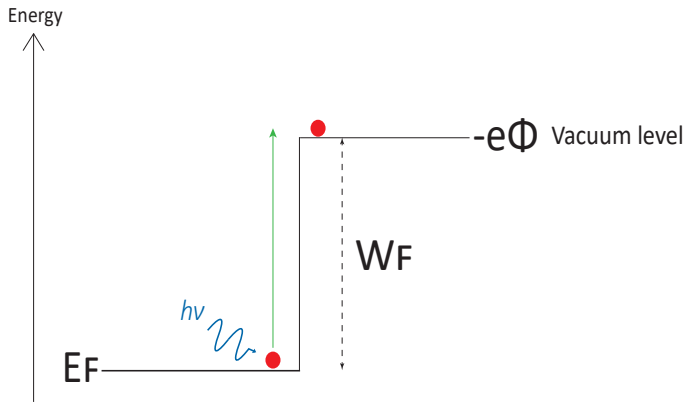

Figure 1: Schematic of linear emission with $h\nu \geq W_F$.

2.2 Non-linear photoemission

Electron photoemission is possible even when the electromagnetic radiation striking the material has lower energy than the potential barrier the electron encounters ($h\nu \leq W_F$). However, this non-linear effect is observable only at high optical intensities, owing to the anharmonic binding potential of the crystal structure. For a plane wave or a Gaussian beam, the intensity I is proportional to the square of the electric field E:

$$I = \frac{c\varepsilon_0 n}{2}|E(t)|^2 \tag{1}$$

In the above expression, c represents the speed of light in free space, ε_0 is the vacuum permittivity, n is the refractive index, $E(t)$ is the time-dependent electric field described in eq. 4 (presented in the following chapter). Therefore, in order to achieve a noticeable non-linear effect, the electric field peak on the material must be sufficiently high. To meet this condition, Field Enhancement (FE) mechanisms such as plasmonic resonance and geometrical resonance prove useful in enhancing light-matter interaction and concentrating light within a small volume region.

Furthermore, the use of a pulsed laser can also be exploited to achieve high electric field peaks. Unlike continuous wave lasers, pulsed lasers generate a train of pulses with a specific duration and repetition rate, rather than emitting continuously. The power of each pulse is determined by the ratio of the average power to the repetition rate, resulting in the attainment of high instantaneous electric fields (in comparison to a continuous wave laser with the same average power) [Fig. 2].

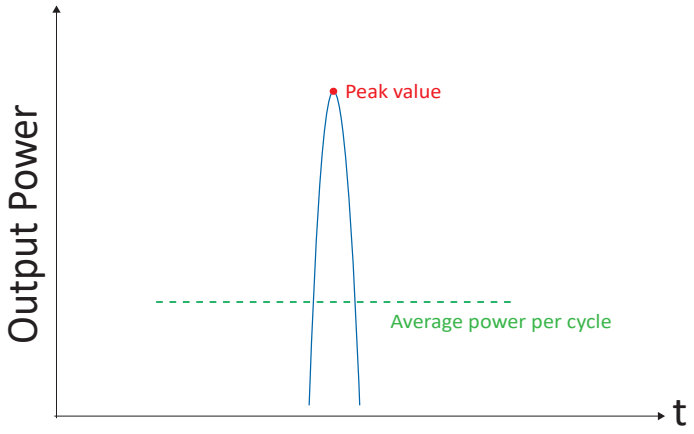

Figure 2: Pulsed laser output power.

Electron photoemission in the non-linear regime is supported by two distinct physical mechanisms: *multiphotons emission* and *optical-field-driven tunneling emission*.

The first mechanism involves the absorption of multiple photons to surmount the potential barrier experienced by the electron:

$$n \times h\nu \geq W_F$$

. Here, n represents the number of photons absorbed to eject the electron from the material [Fig. 3]. Given that the absorption of photons must align both temporally and spatially to facilitate the occurrence of non-linear transitions, this absorption phenomenon is proportional to the n^{th} power of the optical intensity. This underscores the requirement for a high electric field to truly observe non-linear optical phenomena.

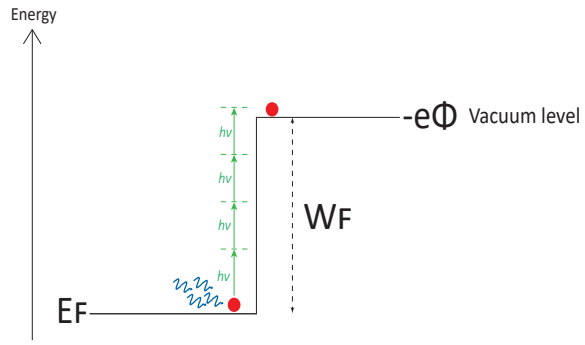

Figure 3: Example of 4 photons absorption

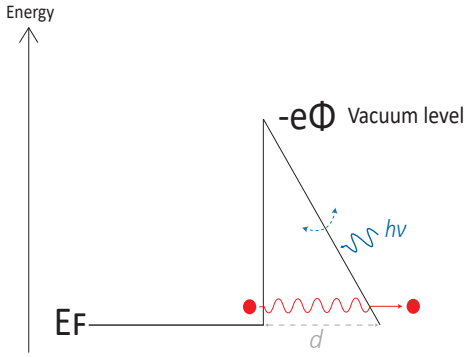

Figure 4: Example of optical-field-driven tunneling

Conversely, the second scenario involves a tunneling mechanism prompted by the modulation of the potential barrier due to the influence of the oscillating incident electromagnetic wave. To be specific, the electron's tunneling through a barrier despite not possessing sufficient energy to surmount it can only be explained from a quantum mechanical standpoint. By addressing the Schrödinger equation within the framework of the electron's wave nature, a finite probability of tunneling emerges. This probability depends on the potential barrier's height, the tunneling particle's mass, and the barrier's width (the latter being the physical property that changes during interaction with the oscillating incident pulse). To solve the

Schrödinger problem, a semiclassical approach (Wentzel–Kramers–Brillouin approximation) is adopted along with an assumption of a triangular shape for the tunneling barrier:

- The wavefunction, characterizing the quantum state of the electron, adopts an exponential form. This approximation holds when the amplitude and phase of the wavefunction evolve gradually.
- The energy barrier is characterized as $-e\Phi(x) = -e\Phi_0 - eFx$, where $-e\Phi_0$ is the height of the unperturbed barrier, and F represents the local electric field.

Through integration across the barrier, and considering a correction factor ν evaluated following the Wentzel–Kramers–Brillouin theory, the transmittance T is determined as:

$$T \propto exp(\alpha(\Phi_0, F)) \quad \text{with} \quad \alpha = \frac{\nu(\Phi_0, F) 4\sqrt{2m_{el}}\Phi_0^{3/2}}{3e\hbar F}$$

In these expressions, m_{el} and E_{el} denote the electron mass and energy within the material, respectively. Tunneling from the distorted barrier then becomes possible and is driven by the potent electric field that interacts with the material. The slope of the triangular barrier follows the oscillations of the incident electromagnetic pulse. During positive sub-cycles, the barrier is enlarged, whereas, during the negative phase, the barrier's width (d) reduces. This consequently heightens the tunneling escape probability, leading to a substantial current response [Fig. 4].

2.2.1 Tunneling transient time

The evaluation of the timescale over which the tunneling event occurs is a dynamic problem because the potential barrier is continuously modulated by the electric field of the incident pulses. However, it is possible to solve the problem at the specific time at which the barrier is shortest (as depicted in Fig. [4]) considering the following constraint: the tunneling event τ_t has to be faster than half of the oscillating period (τ_{crit}) of the barrier modulation $\tau_t \leq \tau_{crit}/2$. This limitation is necessary to solve the stationary problem because otherwise the barrier would not be reduced and the schematic in Fig. [4] not valid anymore.

τ_t can be derived as the ratio between the distance (d) to cross and the velocity (v) of the electron. d is modulated by the intensity of the electric field (F_0) trough the relation $d = W_F/eF_0$, v is instead extracted solving trough the semicalassical approach mentioned above $m_{el}v^2/2 \approx W_F$.

Solving the equation for τ_{crit}, we obtain the timescale within the tunneling event occurs:

$$\tau_{crit} = \frac{\sqrt{2m_{el}W_F}}{eF_0}$$

In this context, F_0 represents the local electric field on the material, which might differ from the driving pulse's E_0 due to the Field Enhancement (FE) phenomena (the explicit relationship between these physical quantities will be discussed later). This inverse relationship between the transit time and the local electric field allows for the reduction of the former by increasing the laser pulse intensity until the condition $\tau_{crit} = \tau_{cyc} = \frac{1}{w}$ is met. Electric field values surpassing the threshold that satisfies this constraint will lead to sub-cycle photoemission. In this regime, electrons are ejected from the material, following the electric field instantaneously because the tunneling event occurs faster than the oscillation period of the incident pulse.

2.2.2 Non-linear currents

The anticipated output current resulting from non-linear photoemission is dependent on the dominant physical mechanism, be it multiphoton absorption or tunneling. The demarcation between these mechanisms is defined by the Keldysh parameter, $\gamma = \tau_t/\tau_{cyc} = w\sqrt{2m_{el}W_F}/eF_0$. When $\gamma < 1$, the strong-field regime is reached, and the emitted current is influenced by the instantaneous field enhancement.

- Strong-field regime:

$$J_{FN} = a\frac{F_0^2}{W_F}\exp(-vb\frac{W_F^{\frac{3}{2}}}{F_0}) \qquad \text{if } \gamma < 1 \tag{2}$$

- Multiphoton regime:

$$J_{MP} \propto |F_0|^{2n} \qquad \text{if } \gamma > 1 \tag{3}$$

Here, a,b, and v are correction coefficients accounting for the potential barrier's height and shape.

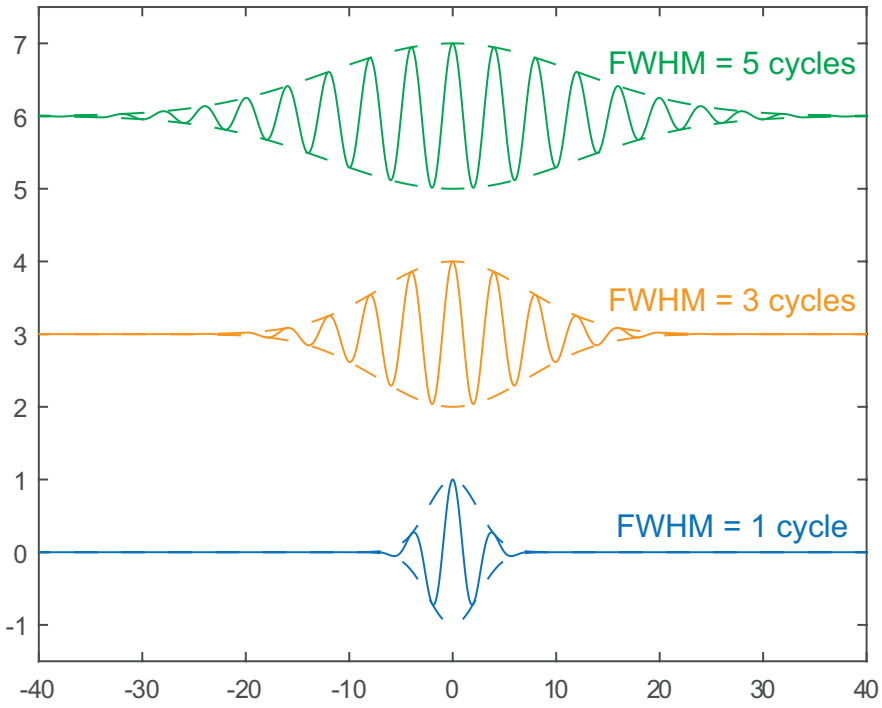

Figure 5: Pulses with different FWHM (normalized to 1)

3 Few-cycle waveforms and CEP

The electric field of the laser pulse that illuminates the device can be modeled as the product of a cosine signal and an envelope:

$$E(t) = A(t)E_0 cos(wt + \phi) \tag{4}$$

Here, $A(t)$ represents the time-dependent envelope, E_0 is the peak electric field, w is the central frequency of the electromagnetic radiation, and ϕ is the carrier-envelope phase (CEP). For long pulses, the CEP is often not relevant as it would have little impact on any measurable quantity. However, for few-cycle optical pulses, the CEP can drastically reshape the field. In this work we leverage this field reshaping and its impact on the photoemitted current to develop devices for detecting CEP.

The envelope, which can take shapes like Gaussian or cos^2, is defined by the full width at half maximum (FWHM) parameter. This parameter measures the distance between two points at which the function reaches half of its maximum value, providing information about the width of the envelope. Based on this parameter, the pulse will contain a certain number of cycles [Fig.5].

As depicted in [Fig.6], different pulse shapes exist for a certain envelope and depend on the value of ϕ. This work aims to develop a silicon detector capable of discriminating the CEP of the incident pulse that triggers the optical field-driven tunneling emission.

3.1 Carrier-envelope phase sensitivity

A device operating in the optical-field-driven tunneling regime no longer responds primarily to the average photon density reaching the material within a pulse cycle; instead, its sensitivity is directed toward the waveform of the electric field itself. This assertion becomes clearer

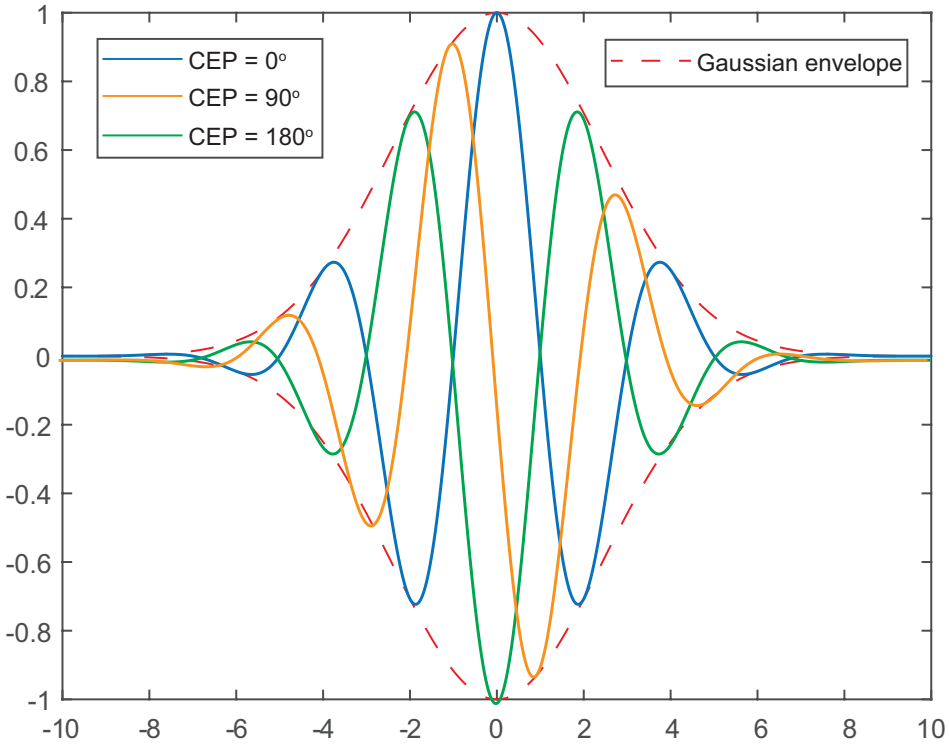

Figure 6: Single-cycle pulse with different CEP (normalized to 1)

upon observing [Fig. 7]. Tunneling current peaks (as described by eq. 2) within the optical-field-driven tunneling regime are juxtaposed with the sub-cycle components of the pulse at varying Carrier Envelope Phase (CEP) values. The total current, derived from integrating the tunneling current components across the pulse's time duration, becomes dependent on the CEP, even when the pulse envelopes remain consistent. Consequently, by measuring the output current, it becomes feasible to discern different CEP values for the incident pulses.

However, the CEP sensitivity vanishes in the multiphoton regime because the absorption phenomenon hinges on pulse intensity. Since only the pulse envelope and its electric field peak contribute to intensity (eq. 1), the CEP signature fades away.

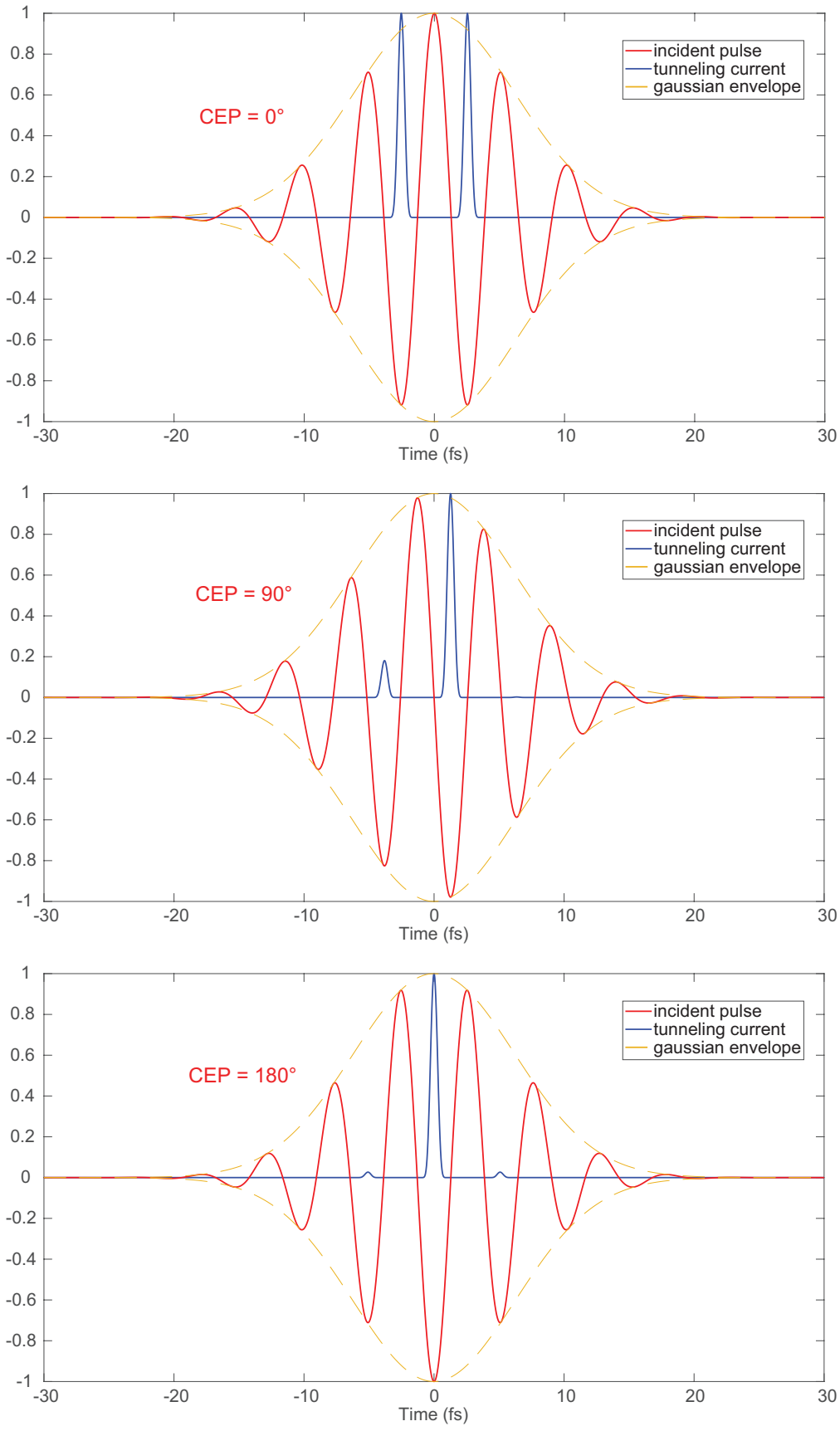

Figure 7: Tunneling current expected for the same envelope with different CEP.

3.2 Carrier-envelope phase detection and stabilization

The interest in detecting the CEP of the incident laser source is related to growing interest in frequency comb source generation. A frequency comb is an optical spectrum composed of equally spaced frequency components associated with a train of ultrashort pulses in the time domain, with a repetition rate determined by the inverse of the frequency components spacing. A perfectly periodic pulse train, both in intensity (envelope) and in electric field (waveform), is obtained if the spectrum is composed of harmonics (integer multiples) of the repetition rate.

However, chromatic dispersion and non-linear phenomena (frequency dependent) cause a shift in the carrier-envelope phase from pulse to pulse of the ultrashort train due to the non-periodic array of frequency components. It is clear that dispersion compensation is necessary to avoid drift of the relative phase between the comb lines and ensure coherence and stability of the comb. This goal is fully reached when no CEP shift between each pulse of the train is observed and the CEP is said to be locked.

The stability, coherence, and precision of the frequency comb generated are then useful in applications related to attosecond science [6], and atomic clocks [7] where the relative timing between ultra-short pulses is critical or to optical frequency synthesis [8], and precision spectroscopy [9] where CEP-locked frequency combs can be easily combined with other laser sources because their phases are synchronized.

4 Nanoantenna optical-field emitters: state of the art

Nanoantennas offer interesting potential for controlling light-matter interactions due to their adaptable geometries. A triangular nanoantenna, for instance, can selectively respond to specific light wavelengths while displaying insensitivity to others, accomplished by simply adjusting its geometric dimensions.

Nanoantennas function as optical-electrical transducers: incoming electromagnetic radiation couples with the resonant modes (dependent on geometry) of the nanoantenna, leading to amplification of the local electric field near the apex region. This phenomenon opens up the opportunity for optical-field-driven tunneling emission, originating from the apex area that encounters field enhancement (FE).

Focusing attention on the CEP detection capabilities of this architecture, an extra layer of flexibility arises from the arrangement of nanoantennas within the array. The average emitted current is defined as the pulse's time-integrated sum of all its sub-cycle components.

- *symmetric configuration*: a pair of triangular nanoantennas is situated in a bowtie configuration, with the apexes facing each other [3] [4]. Emissions can occur in both directions:
  - negative sub-cycle pulse components (depicted in blue) facilitate tunneling from the left nanoantenna to the right one due to barrier reduction. Conversely, electrons from the right-side nanoantenna encounter an elevated barrier, precluding tunneling within the bow-tie gap.
  - Positive sub-cycle pulse components (shown in red) manifest the opposite behavior. Electrons from the left nanoantenna struggle to tunnel out due to barrier elevation, while the electrons in the right nanoantenna encounter a diminished barrier, contributing to tunneling from right to left.

  The collected average current (time-integration of the dashed blue and red components in the figure) varies from [-max,+max] relative to the CEP of the incident pulse. The averaged current goes to zero at the CEP value for which all the positive sub-cycle current components are compensated by the negative ones.

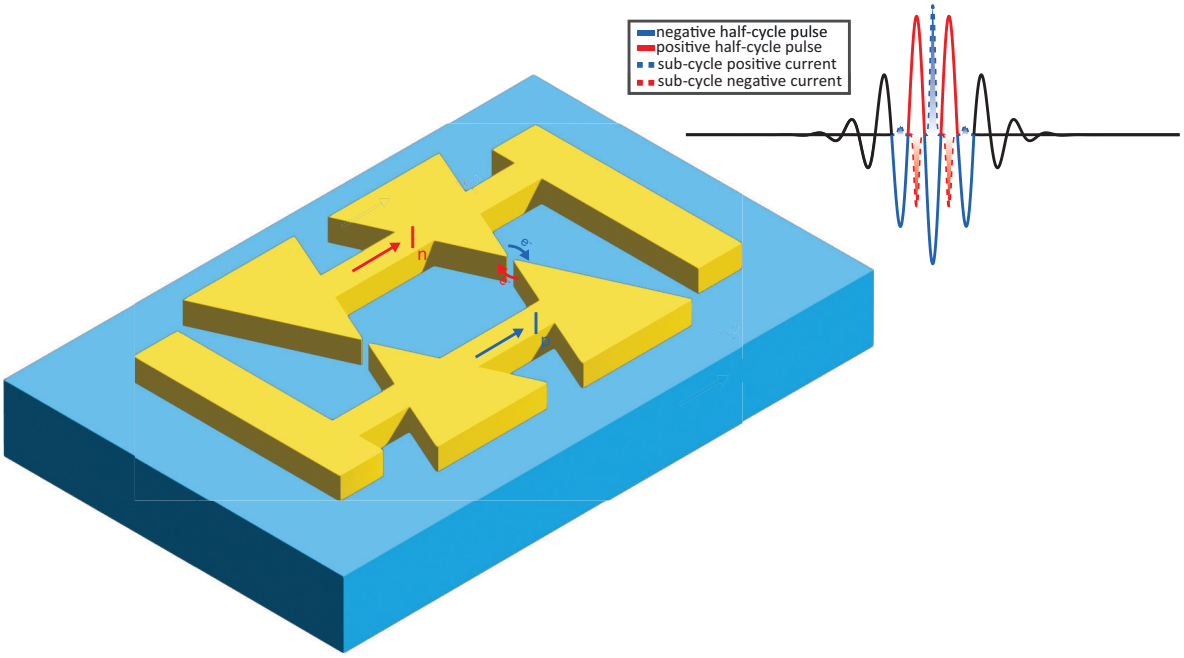

(a) symmetric configuration

- *antisymmetric configuration*: A triangular nanoantenna is positioned facing a flat rectangular wire. This kind of configuration has been investigated for optical field sampling applications [1]. Emission occurs unidirectionally, where the nanoantenna functions as an emitter, while the rectangular wire, not subjected to the same Field Enhancement (FE) as the nanoantenna apex, operates as a collector. Only negative sub-cycle optical pulses have the capability to alter the potential barrier, allowing electrons to tunnel through it. As a result, no response in terms of sub-cycle emission is expected for positive sub-cycle optical pulses.

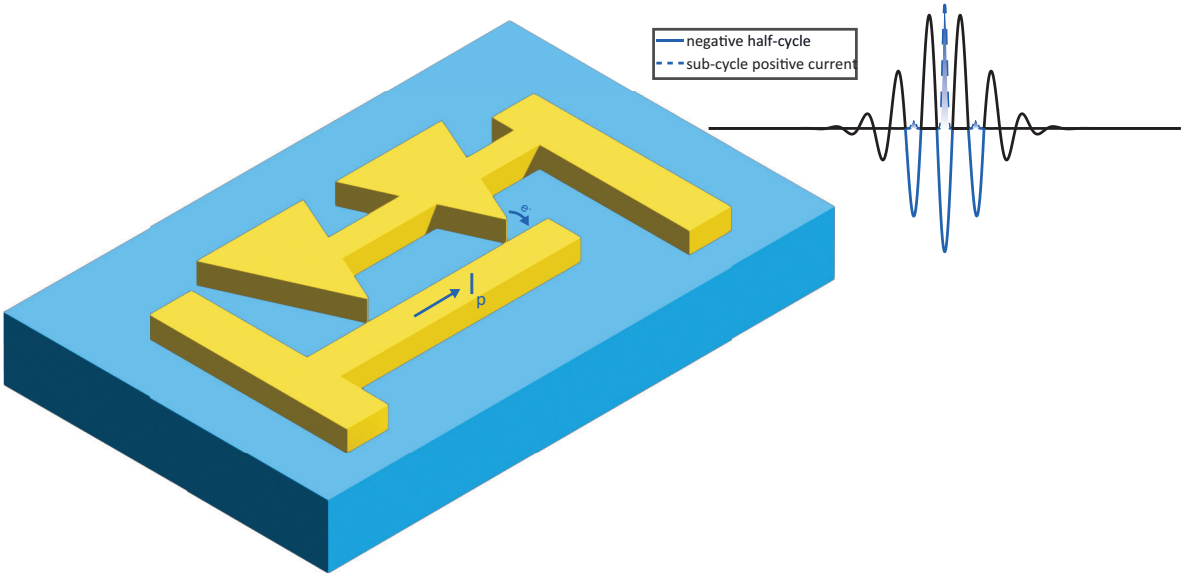

(b) antisymmetric configuration

- *rectifying configuration*: a pair of triangular nanoantennas is arranged in a back-to-back configuration. One nanoantenna will emit at a time, contingent upon whether it

is a positive or negative sub-cycle optical pulse, with the current polarity consistently maintained [10]. Notably, the nanoantennas continually function as electron emitters, while the wires serve as collectors. While this configuration may compromise CEP sensitivity, as both positive and negative sub-cycles contribute to amplifying a positive current, it boasts a greater magnitude in terms of output value.

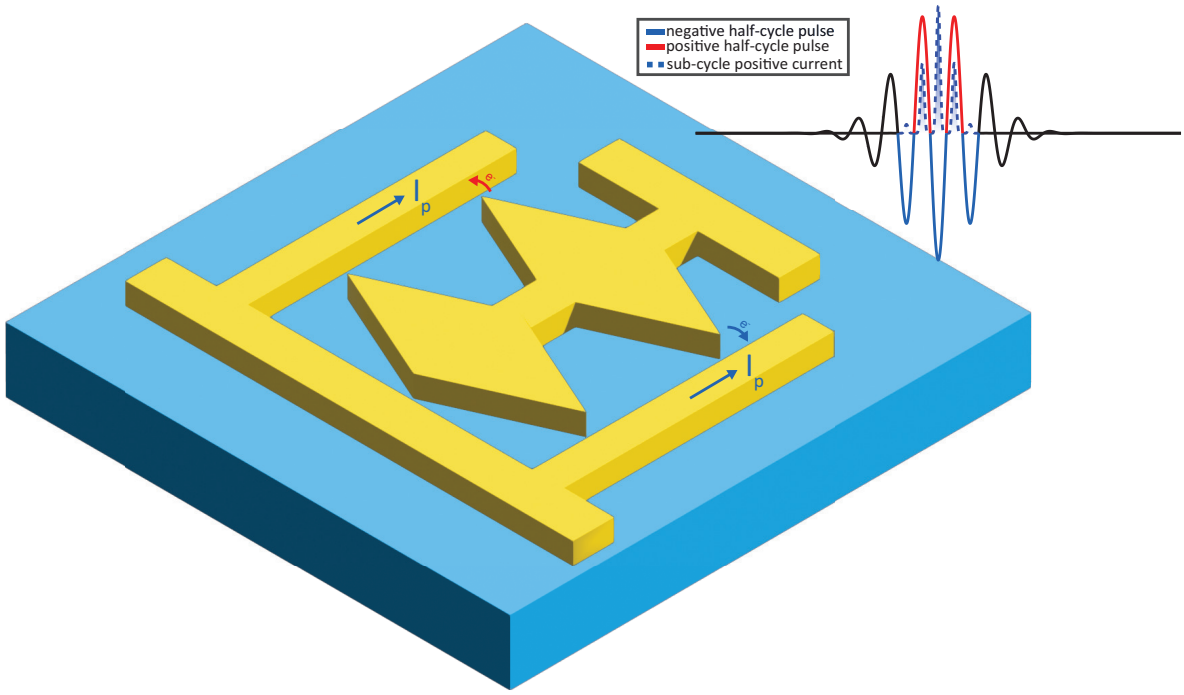

(c) rectifying configuration

4.1 Gate pulse degree of freedom

In the literature, the carrier-envelope phase (CEP) sensitivity range is commonly discussed for pulses containing up to 5 cycles. For pulses with a larger number of cycles, the carrier signal starts to resemble the envelope, and the relevance of CEP sensitivity diminishes.
Within the Fabry-Perot cavity of the laser system, multiple longitudinal modes can coexist. These modes possess the potential to interfere, leading to the laser output adopting a pattern with a certain periodicity. By establishing a fixed phase relationship between these modes, moments of constructive and destructive interference can be achieved, thereby generating the periodic train of pulses. Moreover, the NPE system incorporates a *polarizing beam splitter (PBS)*, which provides a linearly polarized output pulse. The quantity of frequency modes implicated in the interference mechanism influences the pulse's temporal extent. As this quantity increases, shorter pulses are produced.

4.2 Materials and geometrical design

The design of the nanoantennas is asymmetric, ensuring the exploitation of the Field Enhancement (FE) mechanism specifically in the apex region near the gap. In this context, the backside of the triangle does not encounter a high local electric field and thus does not facilitate photoemission.

Furthermore, to induce the correct bending of the potential barrier for electron tunneling out, the electric field must oscillate along the height axis of the triangle. This characteristic makes the triangular nanoantenna devices polarization-sensitive. Electric field oscillations in

other directions do not cause the bending of the potential at the material/vacuum interface, a crucial factor in reducing the barrier's width and achieving a significant escape probability.

As detailed in [1] and [3], the feasibility of fabricating these nanostructures with a nanometer-scale gap presents promising prospects for operating the devices under ambient conditions (without requiring vacuum equipment) and at low voltages. The narrow width of the tunneling barrier (shorter than the electron mean free path) ensures fast electron transit times and minimal interaction with gas molecules.

Metallic plasmonic materials have been investigated to exploit FE in nanoantenna arrays, primarily due to their high plasma frequency f_{pe} that extends into the near-infrared/visible range. For frequencies below f_{pe}, these materials exhibit negative real permittivity and can sustain plasmonic resonance. This characteristic arises from the abundance of free electrons within the material, making metals the historical preference for such applications. *Gold* emerges as a suitable candidate for plasmonic nanoantenna applications due to its chemical inertness in environments like air or water. However, its losses increase from the visible to the ultraviolet region. *Aluminum* has a wider plasmonic band, sustaining this resonance up to ultraviolet frequencies, but it rapidly reacts with oxygen. Consequently, its fabrication and overall performance are influenced by the formation of an aluminum oxide layer on its surface.

4.3 Limits

Previous works have demonstrated CEP detection and optical field sampling with nanoantenna arrays [3][4][1]. However, several significant challenges, particularly pertaining to fabrication and reliability, persist.

Degradation of gold devices due to highly localized electric fields and heating has been investigated in literature [11][12]. The strong plasmonic response of the gold thin film is also followed by a non-efficient thermal dissipation that causes degradation and reshaping of these nanostructures. In [11], the gold nanoantennas' plasmonic performance and thermal stability are compared with refractory materials like TiN. The results show that, even at temperatures below the gold melting point, both the plasmonic resonant frequency and the plasmonic coupling intensity vary with temperature. This behavior is, instead, not observed for TiN: the refractory material preserves its plasmonic properties for a higher temperature range. The change in optical properties is related to the reshaping to which the gold nanoantennas are subject.

This thesis is supported by [12], in which gold nanoantennas reshaping is intentionally exploited to change the resonant frequency of the nanoantenna. Mass transfer of gold is induced through the shining of high-energy terahertz pulses on the nanoantenna. The thermal load, caused by the high current density that flows through the material, is not dissipated fast enough. Therefore, it breaks the atom from the structure and generates a flow of mass that follows the current direction. This causes changes in the geometrical shape of the nanoantenna and, consequently, a shift in the resonant frequency.

Moreover, shorted bow-tie nanoantennas are found in gold devices with nominal gaps below 30 nm due to fabrication limitations [3]. To salvage the array's functionality, inspection of all pairs is required, and an electromigration process must be executed to remove the entire column in which the short occurs. Also in this work, variations in gap width emerge after illumination, leading to a shift in the FE spectra.

For all the mentioned reasons, the use of gold as a material to exploit the optical-field-emission tunneling regime is limited to academic research purposes due to unreliable fabrication processes and degradation of plasmonic performances after illumination.

As mentioned before, refractory plasmonic materials like TiN have been explored to solve the challenges related to the use of gold. Bow-tie nanoantennas crafted from doped titanium

nitride can be fabricated, with reported gaps as small as 10 nm [4]. Although this material demonstrates minimal degradation after illumination, it does not grant access to the optical-field-driven tunneling emission regime. Therefore, the investigation of new materials, new designs, and new resonance mechanisms motivates the research statement of this master's thesis.

5 Silicon device

Optical-field-driven tunneling has been previously demonstrated in [5]. In that case, the device was composed of nano-sharp silicon pillars, forming a non-planar array of photo emitters [Fig. 9]. The electron emission process ($\lambda = 800\,\text{nm}$) was possible due to the *FE* at the apex. The goal of the simulations performed in this thesis is to study the feasibility of on-chip Si-based petahertz electronics. In particular, I focus on Si-based optical tunneling devices for the purpose of carrier-envelope-phase detection. To do this we first study the electromagnetic properties of planar Si device arrays similar to the previous gold bow-tie work [3]. The simulations evaluate whether silicon antennas can achieve a similar level of optical field enhancement which is critical for petahertz electronics that can operate at low energies. I simulate optical-field photoemission from the silicon antennas to quantify their carrier-envelope-phase sensitivity and compare it to prior work using gold nanostructures.

To determine the best design to exploit FE, it is necessary to evaluate the physical mechanism that the specific material used can sustain to confine the electromagnetic wave in a small region.

Unlike gold and doped titanium nitride, silicon does not exhibit a plasmonic resonance in the visible to infrared wavelengths due to its positive relative permittivity ε_r. This is because plasmonic resonances require a negative ε_r, which is only found in metals. The ε_r of silicon means that it behaves as a dielectric, and does not support plasmonic resonances. However, in the infrared band and for wavelengths low up to 500 nm, the silicon exhibits low losses for thin structures and can sustain Fabry-Perot-like resonances.

In principle, the imaginary part of the refractive index $(n+ik)$ contributes to an exponential attenuation of the beam intensity ($I(z)$) during the propagation in the material following the Beer-Lambert law:

$$I(z) = I_0 \exp(-4\pi z k(\lambda_0)/\lambda_0) = I_0 \exp(-z/\delta_p(\lambda_0)) \tag{5}$$

Here, $\delta_p(\lambda_0)$ is the penetration depth and it is defined as the depth at which the intensity becomes $1/e$ of the original value (I_0) and z is the distance traveled by the electromagnetic pulse in the material.

However, if $z << \delta_p(\lambda_0)$ the losses are negligible, and the wave travels without attenuation. In Fig.[8] The ratio between the wavelength in the material and the penetration depth $\lambda_0/n(\lambda_0)\delta_p(\lambda_0)$ is investigated. It is clearly visible that for wavelength higher than 500 nm the penetration depth is much bigger than the wavelength in the material. Therefore, devices with thickness around $\lambda_0/n(\lambda_0)$, designed in Chap. 6 can be considered lossless for that specific wavelength.

Through geometrical optimization, resonances can be tailored at specific wavelengths and the FE mechanism is exploited in silicon nanostructures. To have access to the resonant modes, the triangular nanoantenna design described in chap. 4 has to be modified. More specifically, a rectangular part has to be added to the already existing triangular shape in order to exploit the Fabry-Perot behavior in the air/silicon/glass trilayer [Fig. 10]. In this rectangular region the cavity modes are generated, the triangular apex, instead, squeezes the modes toward the air gap and localizes the enhanced local electric field at the interface.

From a technological and commercialization standpoint, silicon has several advantages over plasmonic metals for nanoantennas. First, silicon has a well-established fabrication process that allows for the design of small features, such as reducing the gap between the antennas

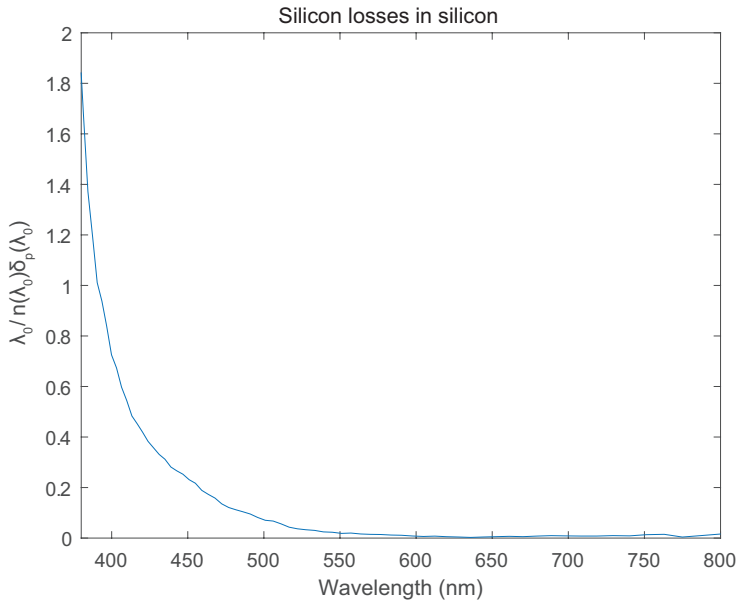

Figure 8: Electromagnetic pulses can propagate in silicon across a distance comparable to the wavelength in the medium without loss.

and increasing the apex angle. Second, the fabrication process for silicon nanoantennas can be commercially distributed in all silicon foundries without any compatibility concerns.

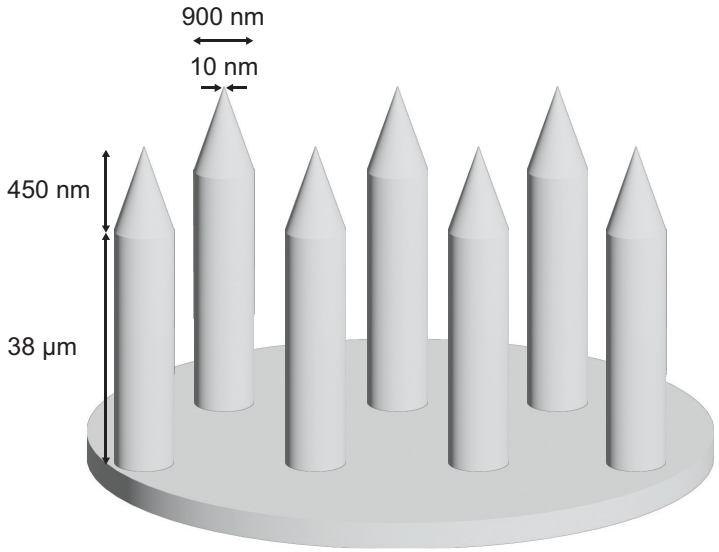

Figure 9: Schematic of silicon pillar array capable of optical-field photoemission

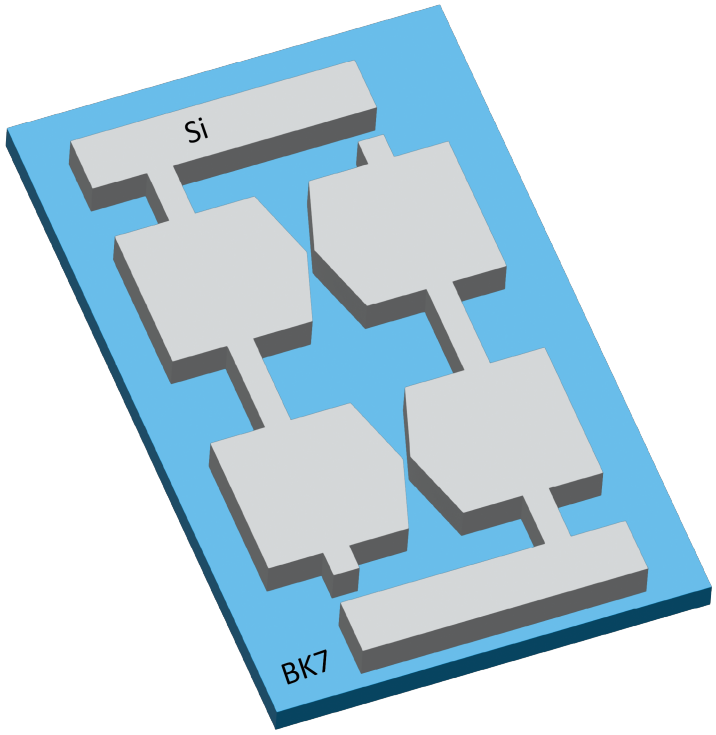

Figure 10: Schematic of the silicon bow-tie array. The nanoantennas and the rectangular contact pads are displayed in gray, the glass substrate is displayed in cyan.

6 Electromagnetic simulations

All the theoretical discussions faced in Chapter 2 are based on the assumption that the nanoantenna material is a metal. Indeed, a band structure in which the Fermi energy (E_F) level is situated in an allowed energy state was postulated. If we are dealing with a semiconductor, the electrons do not occupy the Fermi energy (which is at a specific position within the energy band gap E_G depending on the doping type and level) but rather are located in the conduction band (CB) and in the valance band (VB). Consequently, instead of utilizing the concept of work function, the electron affinity must be taken into account. The latter is defined as the energy difference between the minimum of the CB (MCB) and the level at which the electron is free from the material. With this correction, all the above definitions remain valid even in the semiconductor light-matter interaction.

6.1 Comsol Multiphysics®

Finite Element Method (FEM) simulations are the first step in evaluating the electric field distribution on the material in the light-matter interaction. To achieve this, the commercial software Comsol Multiphysics® has been utilized. The physics integrated into the software package can address the defined electromagnetic study in the frequency domain without requiring extensive computational time. The accuracy of the solutions depends on the precision of the boundary conditions and how fine the computational domain is. Indeed, the FEM analysis transforms the continuous equations of the electromagnetic domain into a discrete set of equations solved for each computational domain (called mesh) that collectively approximate the shape of the geometry.

All the simulations performed are using 3D geometry, following the physics described in the *Electromagnetic Waves, Frequency Domain (emw)* package [13]. The aim is to solve the time-harmonic wave equation to obtain the electromagnetic field distribution. The study conducted is in the frequency domain, with the goal of evaluating the device's response to the impinging plane wave at different wavelengths.

The design of the device is simple and inspired by previous nanoantenna works in which FEM simulations were also conducted [3]. However, in this case, I am interested in understanding the device performance when the gold antennas are replaced with silicon antenna structures, which behave more as a high-index dielectric rather than a noble metal.

The simulated device consists of Bow-tie nanoantenna pairs connected to form an array of photo emitters [Fig. 10]. Due to the periodic boundary conditions set in the simulations, it is sufficient to study the behavior of just one bow-tie pair to extract the *FE* response in frequency. While this approximation is widely used in FEM simulations and it is necessary to avoid unrealistic computational time, it is important to note that the software will simulate an infinite periodic array of nanoantennas pairs, which is not perfectly realistic. We have a finite number of photo emitters on the chip and also some slight geometric differences between each pair due to the fabrication process. This can result in a mismatch between the simulated and experimental data.

6.1.1 Design

A rectangular block of *BK7* (Optical borosilicate-crown glass) was chosen as a substrate. It is widely used in optical applications due to its high transmittance in visible and near-infrared spectra [Fig. 11]. Since BK7 starts to absorb past 2.5 µm, sapphire becomes the optimal choice for situations that demand extensive light transmittance. It facilitates the passage of

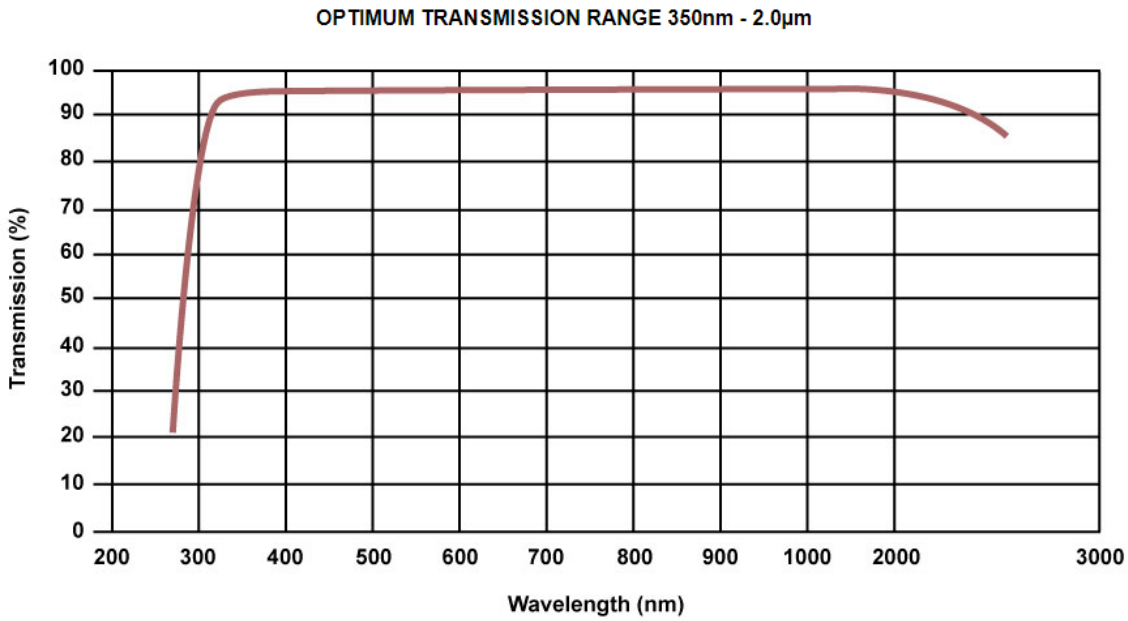

Figure 11: BK7 Transmission range [14]

light across a wide spectrum of wavelengths, spanning from 0.15 to 5 μm – from the vacuum ultraviolet to the mid-infrared spectrum.

Another block with the same dimensions is positioned below the substrate, but in this case, *perfectly matched layer* conditions are applied to mimic a non-reflecting infinite domain. The silicon nanoantennas are placed over the substrate and then surrounded by a block of air [Fig. 12].

The geometry of the silicon nanoantennas is straightforward: a triangular and a rectangular shape are Boolean united and then extruded along the z-axis. To account for the limitations of nanofabrication in etching sharp features, and, therefore, to replicate the expected post-fabrication results, a tip with a radius of curvature of 10 nm is simulated. To do this, a fillet node is applied in the COMSOL Multiphysics® simulations.

To exploit the design's symmetry, the entire geometry has been divided into 4 macroblocks using the $yz-plane$ and $xz-plane$ as dividers. This way, the mesh will initially be generated for just one macroblock and then copied for the others.

Multiple devices were studied, and the dimensions kept constant for all the simulations are reported in Table 1. The reason behind this was to maximize the *FE* at the apex of the prism (at the silicon-air interface). Different configurations for the *triangle height* and *triangle base* have been explored, but the simulated configuration, with a wide apex angle ($\sim 142°$), is the one that ensures the maximum enhancement. The geometric resonance is stronger when the antennas are closer to each other; thus, the value for *gap* was chosen considering the etching limit in fabrication processes (a smaller value was not feasible given the current state of silicon nanofabrication).

6.1.2 Boundary conditions

The optical excitation, depicted in green in Fig.12(b), is simulated by applying *Scattering Boundary Conditions* to the topmost surface. The incident field is modeled as a Gaussian

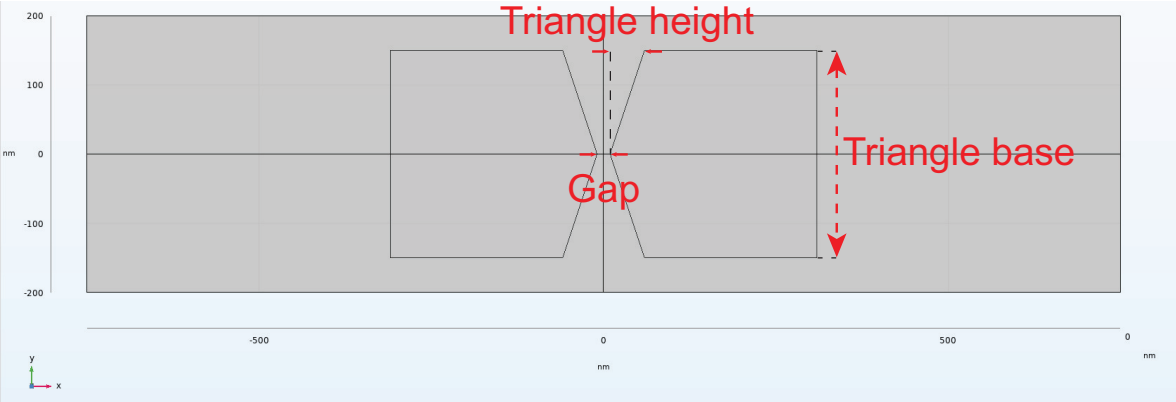

(a) xy-plane view

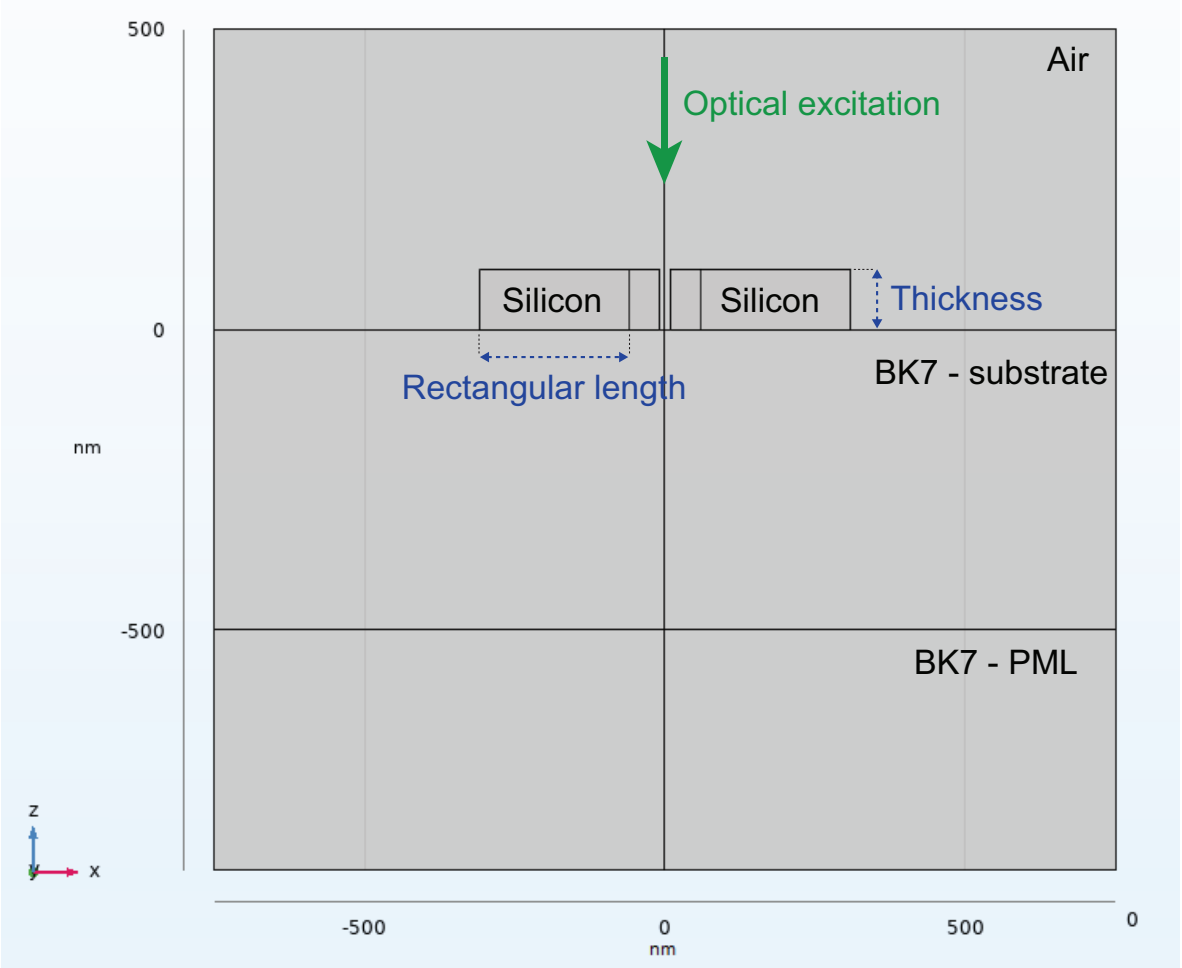

(b) xz-plane view

Dimensions in red are kept constant for all device designs. Dimensions in blue are device-dependent.

Figure 12: COMSOL Multiphysics® design.

Constant parameters	
Dimension	Value
Triangle height	50 nm
Triangle base	300 nm
Gap	20 nm

Table 1: Parameters kept constant for all the design.

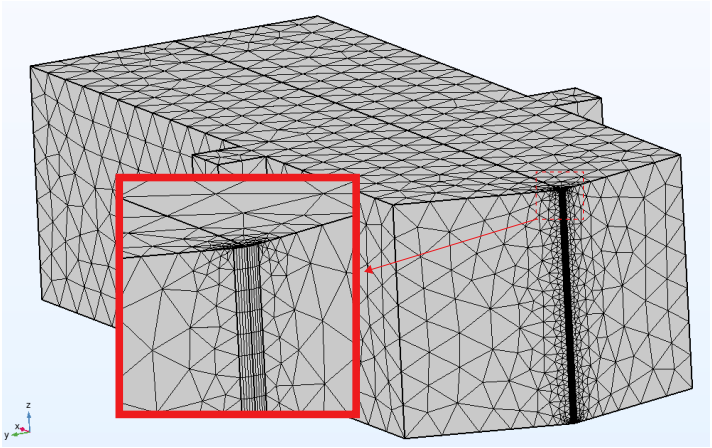

Figure 13: Nanoantenna mesh.

beam with a *Beam radius* large enough to excite multiple nanoantenna pairs simultaneously. Indeed, the actual experimental setup in the laboratory is not advanced enough to selectively excite only one pair of nanoantennas; therefore, the use of this model is well justified. The values for the electric field amplitude (E_x, E_y, E_x) are set to have impinging radiation polarized along the axis of symmetry of the bow-tie (*x-axis*). Finally, to simulate the infinite array of nanoantennas pairs, *Periodic Conditions* are applied to all the remaining rectangular boundary surfaces.

6.1.3 Mesh

The meshing process is not trivial and is often the most time-consuming phase in FEM simulations. In this specific case, meshing was made easier by the presence of planar structures. The use of *Free Tetrahedral* and *Free Triangular* elements as mesh components was sufficient to model nearly all the geometry. The only component that required specific attention was the curved surface at the apex of the triangular. The combination of *mapped* node and *distribution* subnode was sufficient to map the mentioned surface into a regular grid of quadrilateral elements without introducing artifacts [Fig.13].

6.2 Simulations results

The analysis of the *Frequency Domain* studies has demonstrated the possibility of obtaining *FE* even in the non-plasmonic Si structures: the geometry of the silicon nanoantenna can be modified to tune the resonance peak of the electromagnetic field distribution. Depending on the geometry and material of the device, certain frequencies (resonant frequencies) will give rise to standing waves within the nanoantenna. Consequently, specific optical modes become trapped in the device, resulting in the confinement of the electromagnetic field within a defined region [Fig.14]. Due to the wide angle, the optical mode confined in the rectangular region

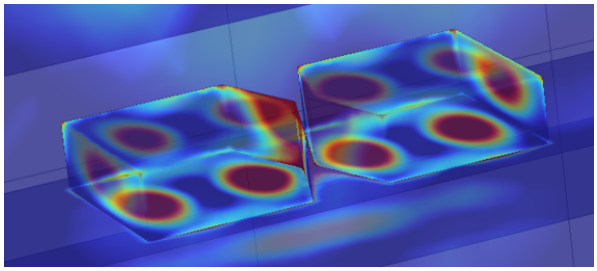

Figure 14: Optical cavity modes inside the nanoantennas pair.

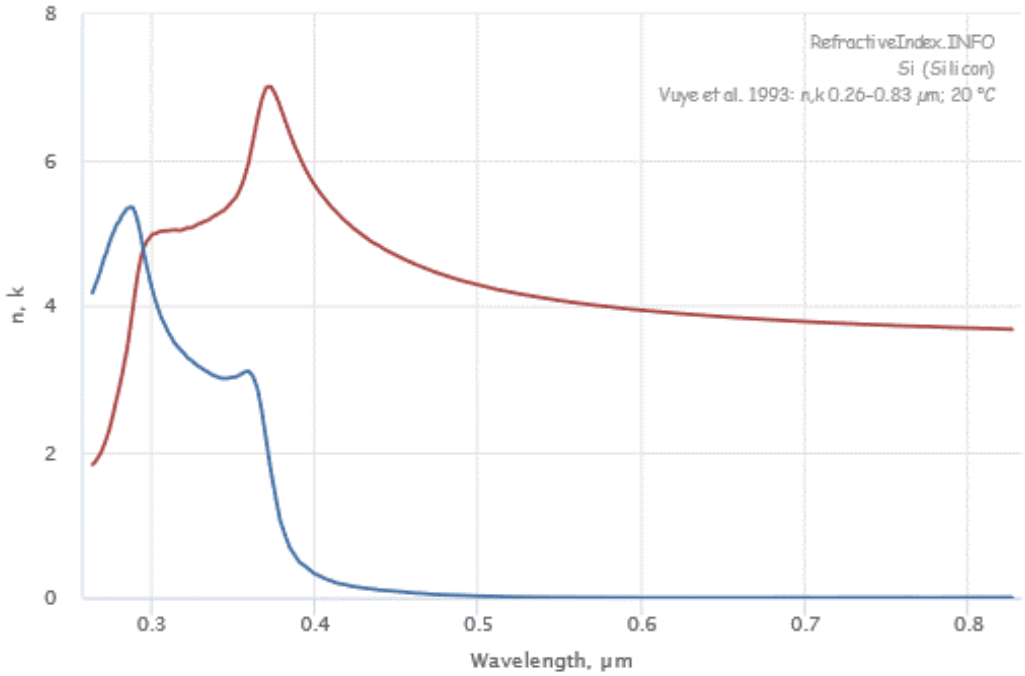

Figure 15: Refractive index and Extinction coefficient for silicon in visible range.

couples to the apex of the triangle, distributing the *FE* across the interface region between the nanoantenna pair. The local electric field at these points will experience enhancement, making it easier for them to enter an optical-field-driven emission regime.

The optical cavity behavior of the device can be justified by two mechanisms:

1. Low losses: The optical pulse is minimally absorbed within the silicon nanoantenna due to its thin geometry and the rapidly diminishing extinction coefficient of silicon above 500 nm [15] [Fig. 15]. This enables the electromagnetic wave to be transmitted across the structure and reach the opposite planar surface.

2. High refractive index contrast: A notable portion of electromagnetic radiation gets reflected at both interfaces, leading to interference between the transmitted and reflected components within the nanoantenna. This phenomenon explains the spatial formation of the resonant modes.

The simulations were conducted in two different spectral regions: *visible* and *near-infrared*. In both domains, the wavelength of the resonance peak depends on two parameters:

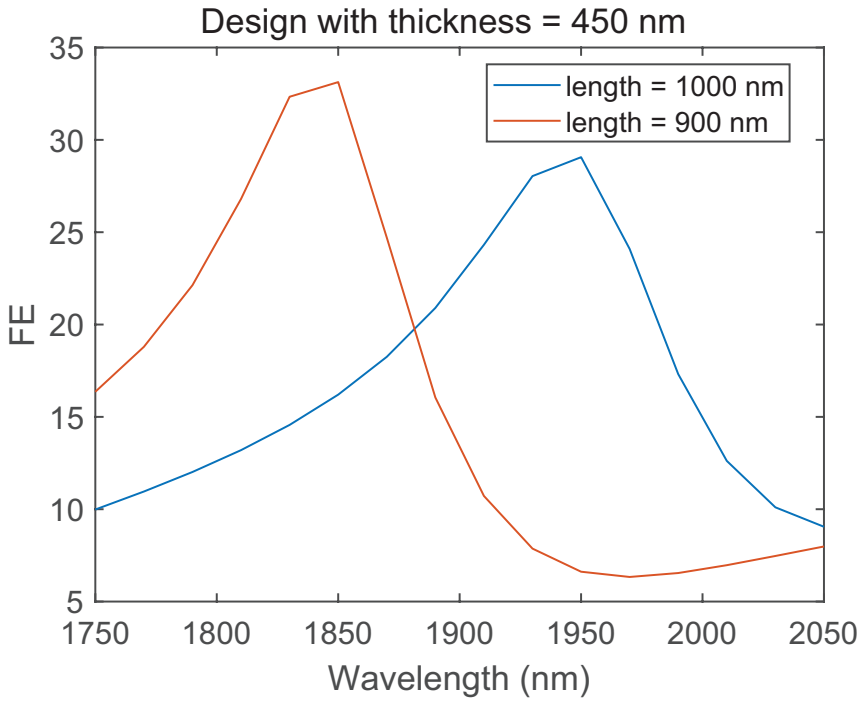

Figure 16: FE at the apex silicon/air interface in the near-infrared region for two different designs

- Thickness, corresponding to the distance between the walls of the cavity, determines the value of the resonance peak and the operational spectral region.
- Rectangular length enables precise tuning of the wavelength of the resonance peak; reducing the length results in a blue shift.

6.2.1 Near-Infrared region

In the near-infrared region, the refractive index of silicon can be approximated as constant for both the real and imaginary parts, without significant error.

To obtain a response from the device, the thickness has been set at 450 nm. In [Fig.16] the FE at the apex is shown for two different Rectangular lengths to demonstrate the tunable property of the device.

Additional designs with a fixed thickness to 600 nm have been simulated to approach higher resonant frequency [Fig.17].

6.2.2 Visible region

In this operational range, the refractive index of silicon does not remain constant with the frequency of the impinging radiation. Therefore, the dispersion relation is to be taken into account. Data points have been sourced from literature [15] for both real and imaginary parts of the refractive index. They are then linearly interpolated within COMSOL Multiphysics®.

Simulations have indicated that a thickness value of 100 nm is appropriate for achieving FE at the apex of the nanoantenna within the visible region. The Rectangular length is subsequently adjusted to finely shift the wavelength at which resonance occurs [Fig.18].

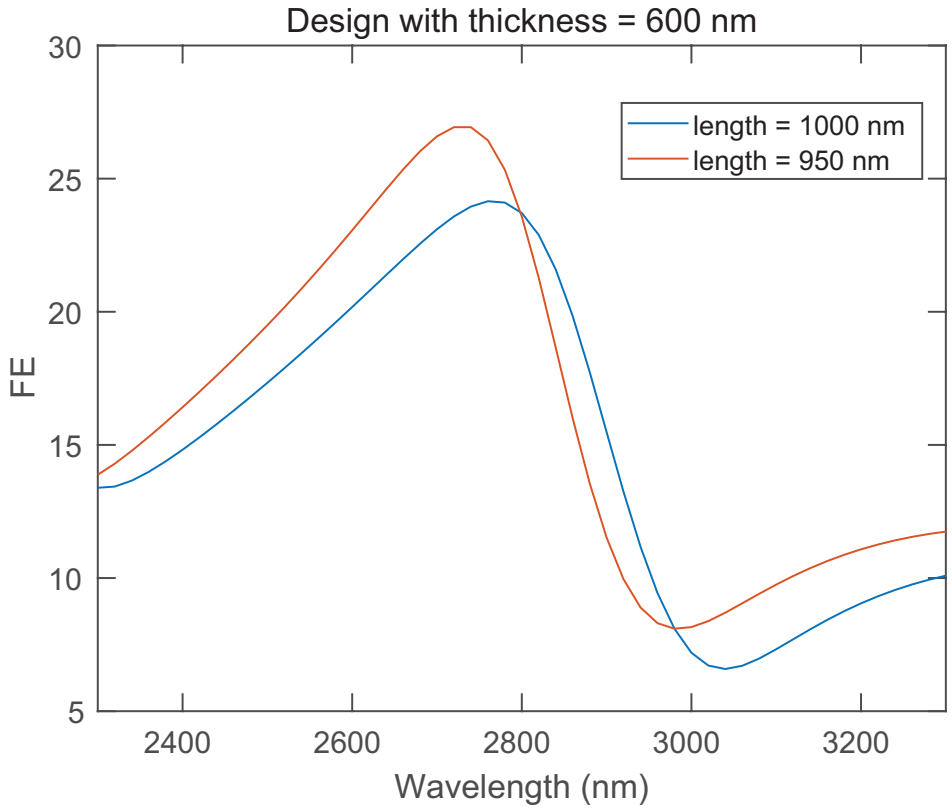

Figure 17: FE at the apex silicon/air interface in the near-infrared region for two different designs

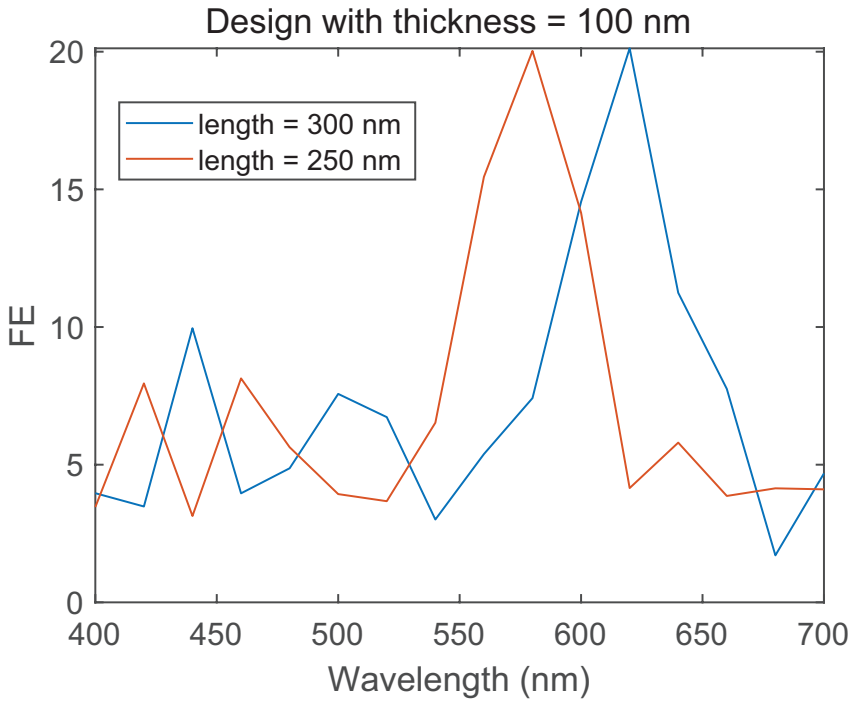

Figure 18: FE at the apex silicon/air interface in the visible region for two different designs

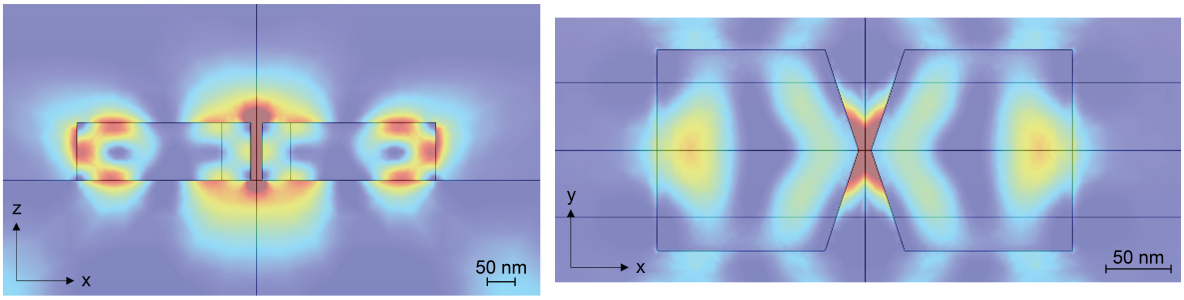

Figure 19: EM distribution at the resonant frequency

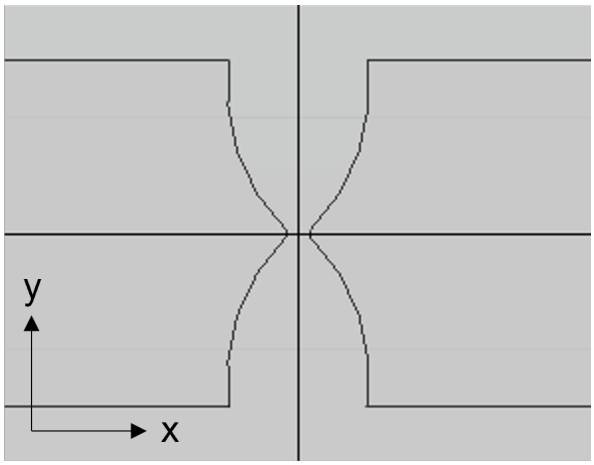

Figure 20: Teardrop shape of the apex

6.3 Transmission wires

FE spectra are initially extracted for bow-tie nanoantennas not connected to form an array [Fig. 12]. The study conducted in the *Frequency domain* reveals the spatial distribution of the electromagnetic field, and due to the behavior of the optical cavity, nodes also form within it[Fig. 19]. In these regions (indicated in dark blue), the total electric field magnitude matches that of the impinging pulse (with a unitary FE value). These regions can serve as suitable locations for placing connecting wires to avoid disrupting the cavity modes. Simulations of connecting wires positioned differently from the optimal configuration have shown changes in FE spectra, including the potential complete disappearance of the enhancement. This result aligns with previous work on plasmonic nanoantennas, where the positioning of wires contributes to the formation of new resonant peaks n. By extending the *Periodic Conditions* previously set to also include the connecting wires, an array of infinite bow-tie pairs is finally simulated.

6.4 Teardrop apex shape

Following the work of [16], other apex shapes were investigated to enhance the device's performance in terms of CEP sensitivity and Signal-to-Noise Ratio (SNR). Rather than simulating a standard triangular apex, a teardrop shape was explored. In this teardrop shape, the lateral sidewalls are modified with a curved line with a variable radius [Fig:20].

In [3], the geometric apex alteration aimed to enhance the Lightning-Rod effect, creating

a sharper apex and thereby achieving higher field enhancement (FE). In this current work, the ultimate goal remains the same. However, the rationale behind investigating the teardrop shape is different: the resonant modes originate and are spatially confined within the rectangular region. Exploring this alternative shape aims to increase the coupling between the optical mode and the apex without disturbing the mode formation.

As indicated by simulations, a meticulous optimization of the teardrop shape can enhance the FE at the silicon/air interface for all the previously proposed designs. A noteworthy finding is that each design requires a distinct radius of curvature (ranging from 80 nm to 200 nm) for the sidewalls to attain maximum FE. The reasons for this outcome still need further investigation, but one hypothesis is that the distinct spatial regions in which the modes are trapped for each design contribute to this variation.

- Design with thickness 450 nm, length 1000 nm and radius of curvature 170 nm.

  FE $\approx$ 34 at the apex silicon/air interface [Fig.21]

- Design with thickness 450 nm, length 900 nm and radius of curvature 180 nm.

  FE $\approx$ 35 at the apex silicon/air interface[Fig.22]

- Design with thickness 600 nm,length 1000 nm.

  FE $\approx$ 27 at the apex silicon/air interface and radius of curvature 190 nm [Fig.23]

- Design with thickness 600 nm, length 950 nm.

  FE $\approx$ 35 at the apex silicon/air interface and radius of curvature 130 nm [Fig.24]

The interesting result from this analysis is that we are able to reach FE factors in silicon nanoantennas comparable to those of bow-tie devices based on plasmonic materials [3][4]. The physics mechanisms behind the resonance are different, but the planar nanoantenna arrays can sustain high local electric field also in dielectric materials.

Finally, it is interesting to notice that for all the designs, the teardrop apex shape contributes to an increase in the FE, but it also causes a shift toward smaller wavelengths in the central resonant peak. This blue-shift phenomenon could be correlated with a decrease in the total length of the device in the regions further from the center part. This correlation aligns with the general tunability properties already described for this kind of device.

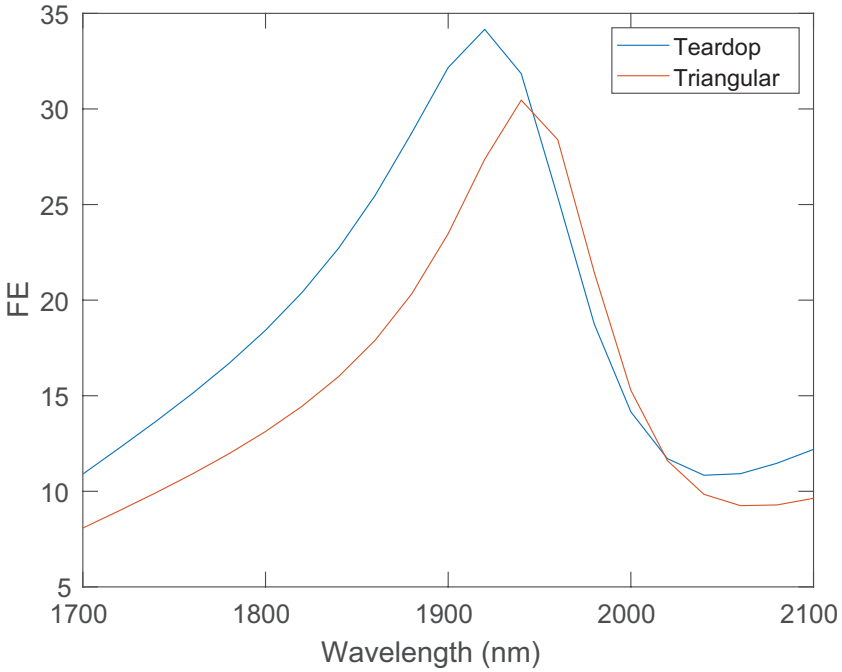

Figure 21: FE comparison for teardrop and triangular apex for central peak 1940 nm

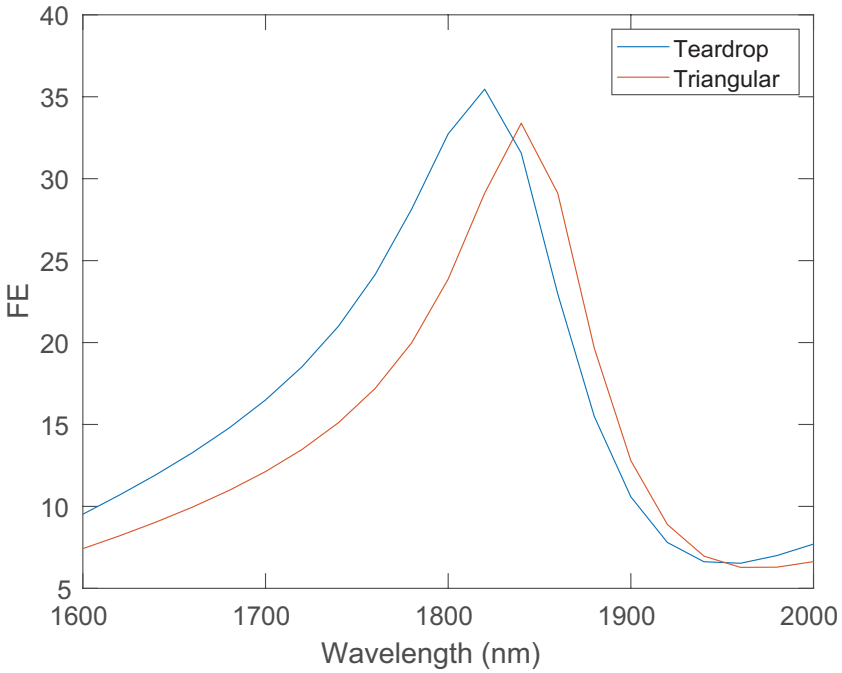

Figure 22: FE comparison for teardrop and triangular apex for central peak 1840 nm

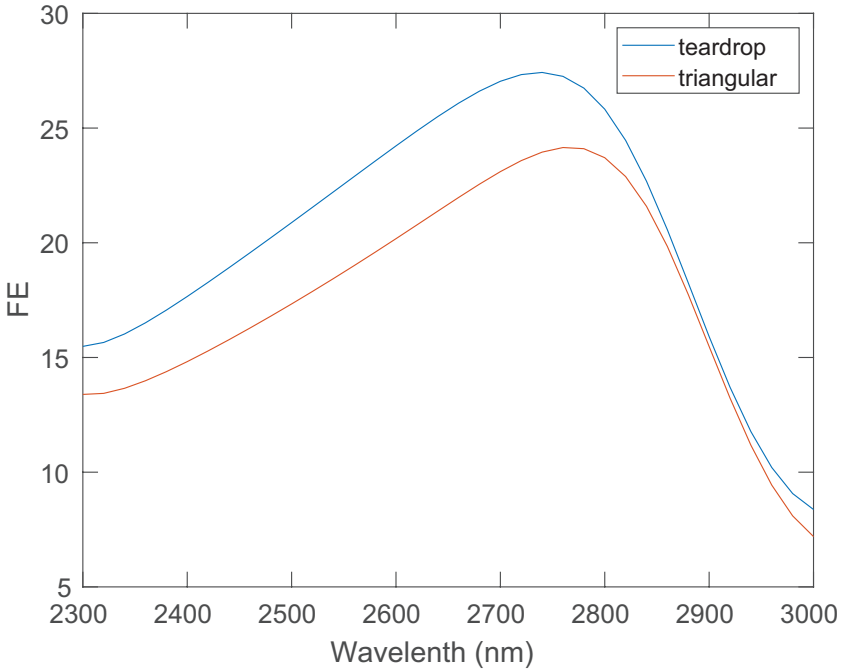

Figure 23: FE comparison for teardrop and triangular apex for central peak 2760 nm

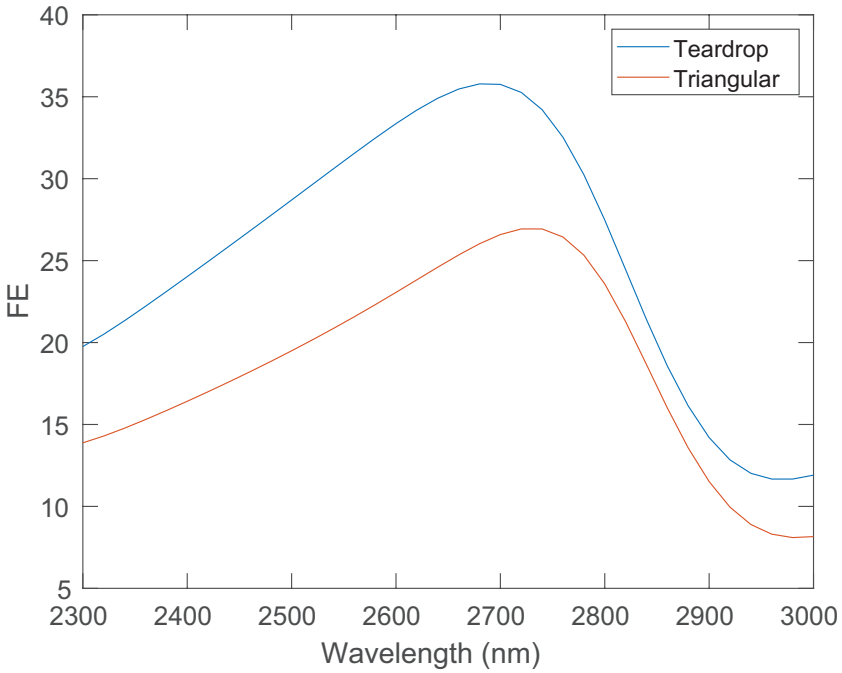

Figure 24: FE comparison for teardrop and triangular apex for central peak 2720 nm

7 Optical field emission

7.1 Time domain analysis

All the results from COMSOL Multiphysics® are extracted in the Frequency Domain. However, in order to simulate the device response to an optical pulse excitation and to model it through the optical-field-driven tunneling current, it is necessary to work in the Time Domain. The local electric field on the silicon device has to be computed, taking into account the simulated FE, and then the photocurrent can be estimated using eq 2.

7.1.1 Discrete Fourier Transform (DFT)

The relationship in the time domain between the local electric field and the impinging pulse can be described by the following relationship:

$$F_0(t) = E(t) * h(t) \tag{6}$$

The electric field of the optical excitation, $E(t)$, is modified as it interacts with the silicon nanoantenna pair, $h(t)$. This phenomenon gives rise to the local electric field, $F_0(t)$.

Evaluating the convolution integral might be challenging, but it simplifies to a point-wise multiplication when moving from the time domain to the frequency domain. Taking the Fourier Transform of the two convoluted components, eq 6 becomes:

$$\tilde{F}_0(\omega) = \tilde{E}(\omega) \times \tilde{H}(\omega) \tag{7}$$

$\tilde{H}(w)$ represents the response of the device in the frequency domain, corresponding to the FE spectrum evaluated in COMSOL Multiphysics® simulations. On the other hand, the Fourier transform of the short pulse in the frequency domain can be computed using the *Discrete Fourier Transform* (DFT) algorithm. An initial MATLAB® code has been used to generate a raised-cosine short pulse (eq 4) with the following parameters:

- Time vector domain: defines the signal's sampling rate in the frequency domain.
- Full width at half maximum (FWHM): determines the envelope's width and the short pulse's time duration.
- Central angular frequency ω: defines the frequency oscillation of the cosine component of the short pulse
- ϕ: CEP of the short pulse

The electric field of the generated short pulse is divided into finite, equally spaced samples and then converted into a complex function in the frequency domain. Consequently, the FE data points extracted from simulations are interpolated at the same sampling points of the short pulse's time-to-frequency conversion to enable point-wise multiplication. The short pulse is simulated with a central wavelength that corresponds to the resonant peak of the FE spectrum [Fig. 25].

The result of the multiplication is the local electric field in the frequency domain. It maintains a cos^2 shape slightly modified by interaction with the silicon nanoantenna. An inverse Fourier transform is applied to this signal, and the real part is extracted to examine the pulse shape at the silicon/air interface and compare it to the original short pulse.

From [Fig. 26], the enhancement of the original black pulse due to the silicon nanoantenna's electromagnetic response is clearly observable. Furthermore, an increase in bandwidth and a Carrier Envelope Phase (CEP) shift compared to the original pulse are seen. These

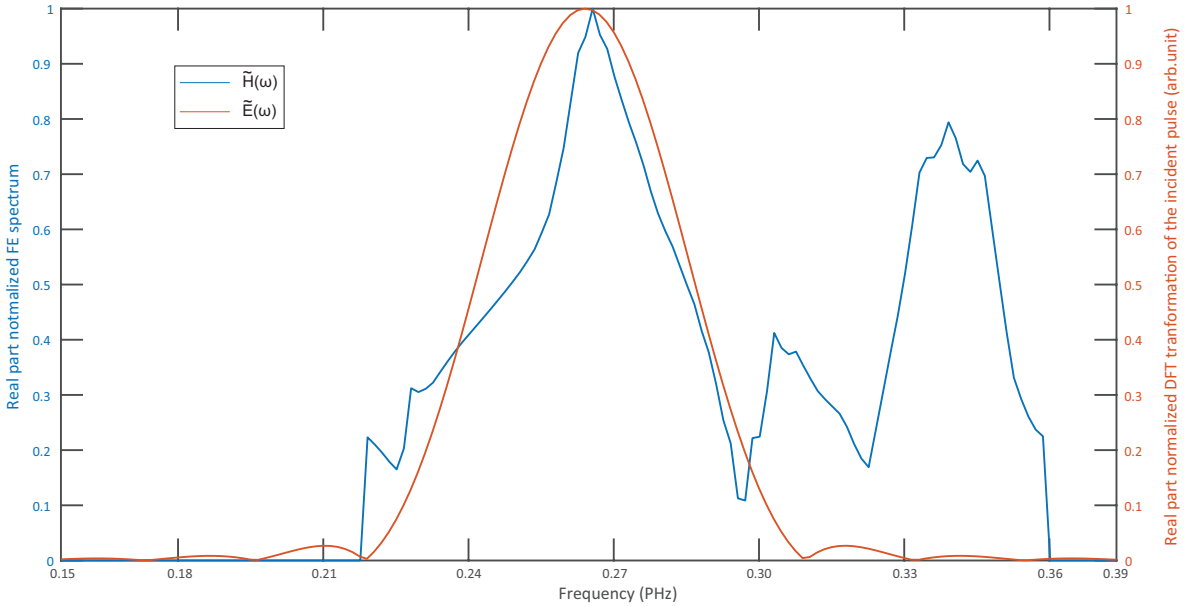

Figure 25: FE spectrum and impinging pulse DFT

effects are consistent with previous research on pulse reshaping in light-matter interaction. Both phenomena are linked to a narrower and asymmetric raised-cosine shape in the frequency domain after interaction with the silicon nanoantenna.

7.1.2 Optical-field-driven tunneling photocurrent

The enhanced electric field is subsequently employed to reconstruct the FN tunneling current expected from the apex point at the silicon/air interface in the time domain driven by the optical field, following eq 2. Symmetric electron emission is assumed to simulate the bow-tie configuration, with an energy barrier of 4.05 eV (Electron affinity for crystalline silicon) as depicted in [Fig. 27].

To assess the photocurrent for varying CEP values and laser power output, two concatenated sweeps are performed:

- $\phi \in (0, 2\pi)$
- $E_0 \in (0.5, 2.5)\mathrm{V/nm}$

Subsequently, the photocurrent components in time are integrated over the pulse's duration to determine the total emitted charge.

7.2 CEP-dependent photocurrent

The objective here is to assess how the electronic performance of the silicon nanoantenna pair changes with the duration of the impinging short pulse and the apex shape. To evaluate the CEP-sensitivity and the theoretically optimum signal-to-noise ratio, the emission from just one nanoantenna in the bow-tie pair is considered, owing to the differential-like electronic circuit of the proposed design. Consequently, only the positive current time components generated from an electric field with a Keldysh parameter lower than 1 are integrated to ensure that we only consider emission within the optical field-driven tunneling emission regime.

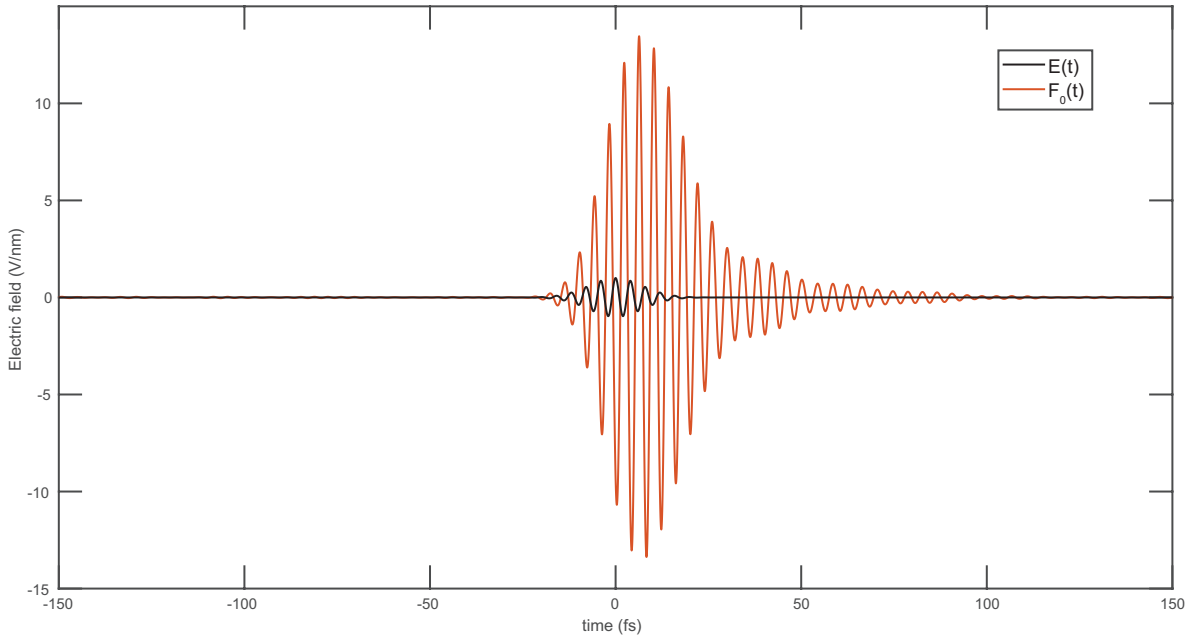

Figure 26: Device response at the apex Si/air interface plotted with the incident pulse waveform.

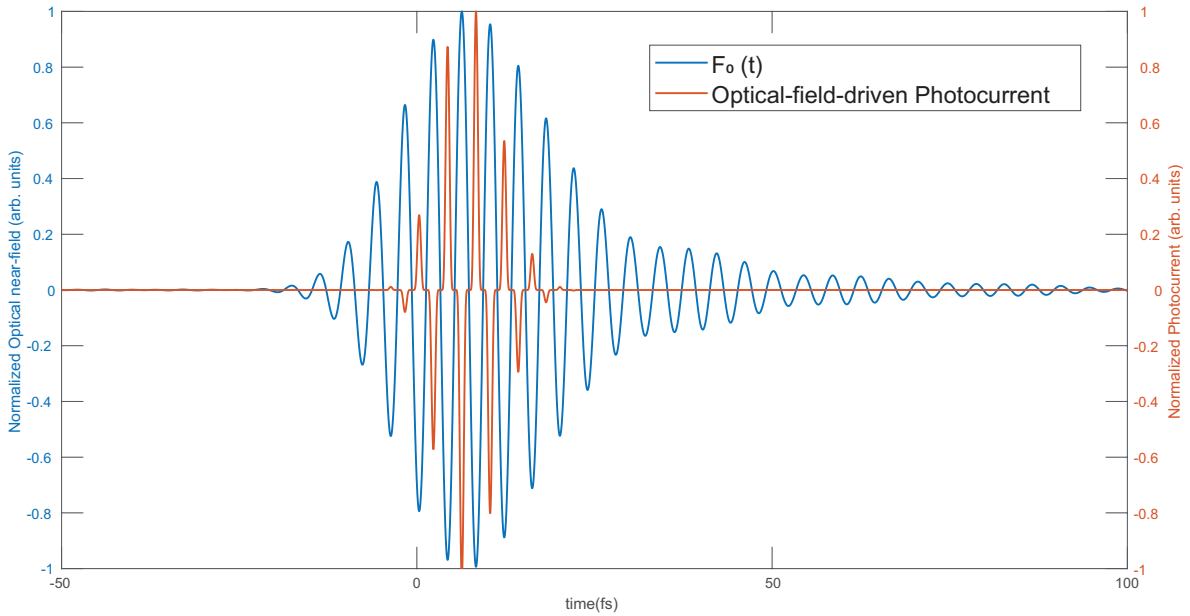

Figure 27: Normalized optical-field-drive tunneling photocurrent.

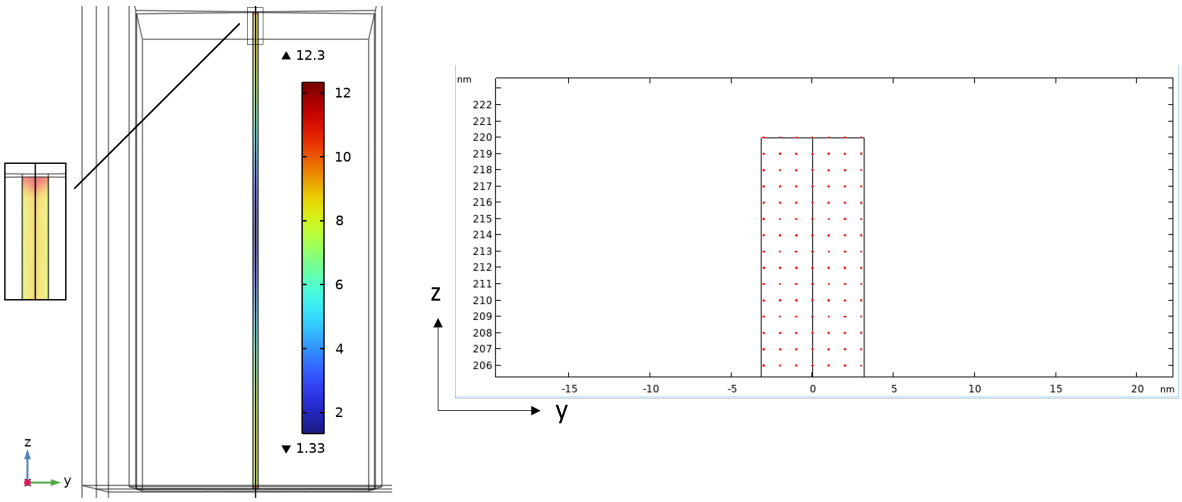

Figure 28: Surface of emission and grid of extraction points.

The area over which optical emission is calculated is the cylindrical surface beneath the rounded apex of the nanoantenna. A grid of equidistant points, each spaced 1 nm × 1 nm on the y-axis and z-axis, is generated on this surface. The FE spectra are extracted for each of these points. The local electric field at each point is evaluated, the FN tunneling current is modeled as described earlier, and the total photocurrent is integrated and summed up [Fig. 28]

The photoemission as a function of the CEP for a specific energy of the laser output is illustrated in [Fig. 29]. A distinctive CEP signature signal is already discernible from this plot. However, to facilitate comparisons across different numbers of cycles or designs, it is essential to evaluate the following physical quantities:

- Q_0: the average photoemitted current per pulse.
- Q_1: the difference between the maximum emission value and the average value. This measurement provides insights into CEP shifts.

7.2.1 CEP sensitivity and Signal-to-Noise ratio

Previous studies have demonstrated the following direct proportionality:

$$\frac{Q_1}{Q_0} \propto \text{CEP sensitivity} \tag{8}$$

$$\frac{Q_1^2}{Q_0} \propto SNR \tag{9}$$

These ratios have been investigated in this work for all the designs outlined earlier, considering both a 3-cycle and a 5-cycle FWHM for the impinging short pulse [Fig.30] [Fig.31] [Fig.32] [Fig.33].

For all the designs, both the CEP sensitivity and the SNR are enhanced for a lower number of cycles in the impinging short pulse. This decrease in performance can be attributed to the following factors:

- An increase in the average photoemitted current (Q0) when the number of optical cycles increases, as more sub-cycle components, leading to optical-field-driven tunneling, are present in the impinging optical signal (as depicted in [Fig.5]).

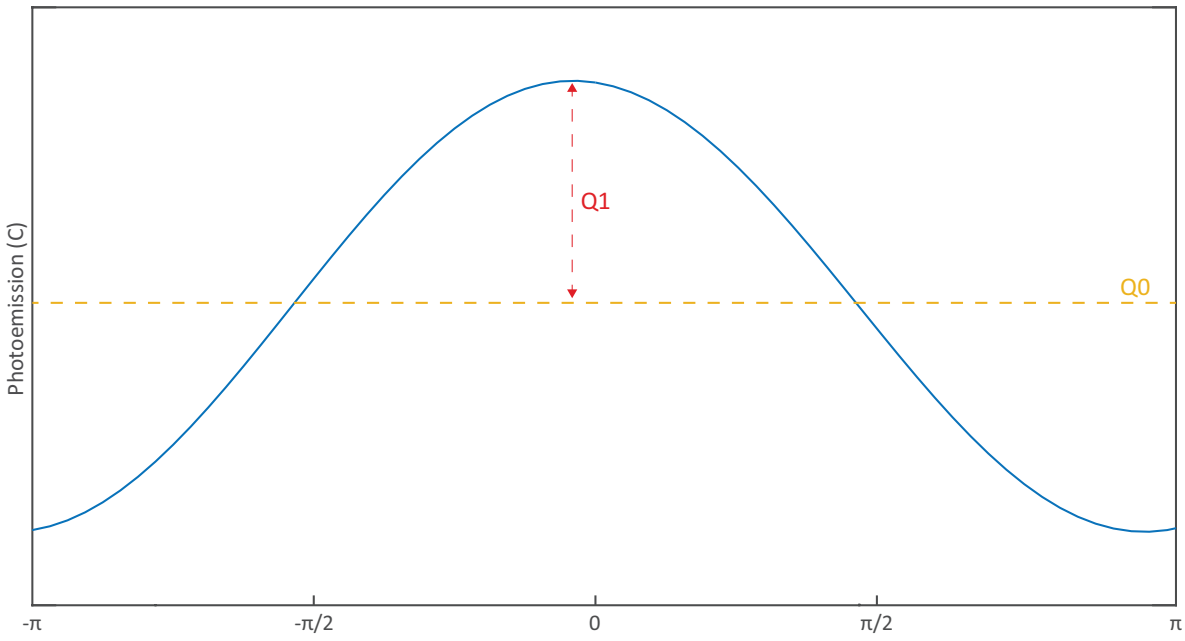

Figure 29: Charge emitted per pulse as function of CEP.

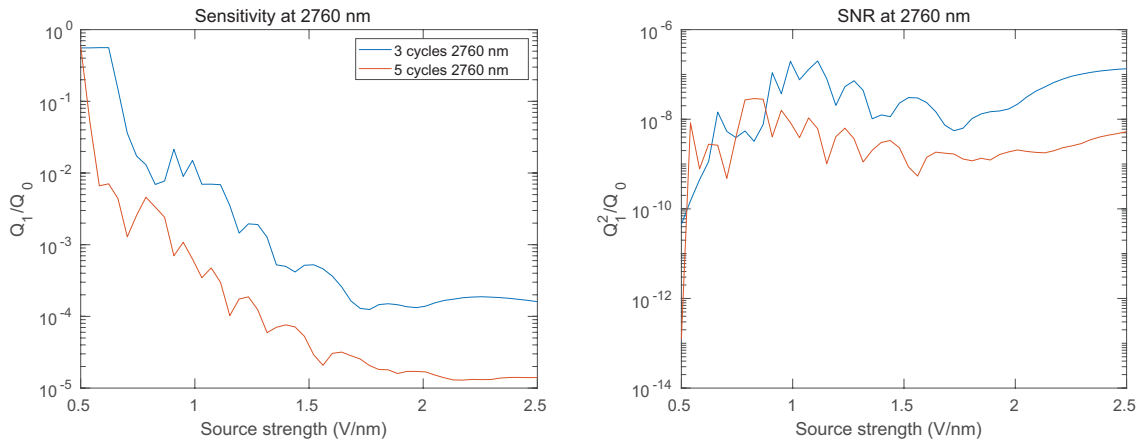

Figure 30: Sensitivity and SNR for thickness = 600 nm and length = 1000 nm

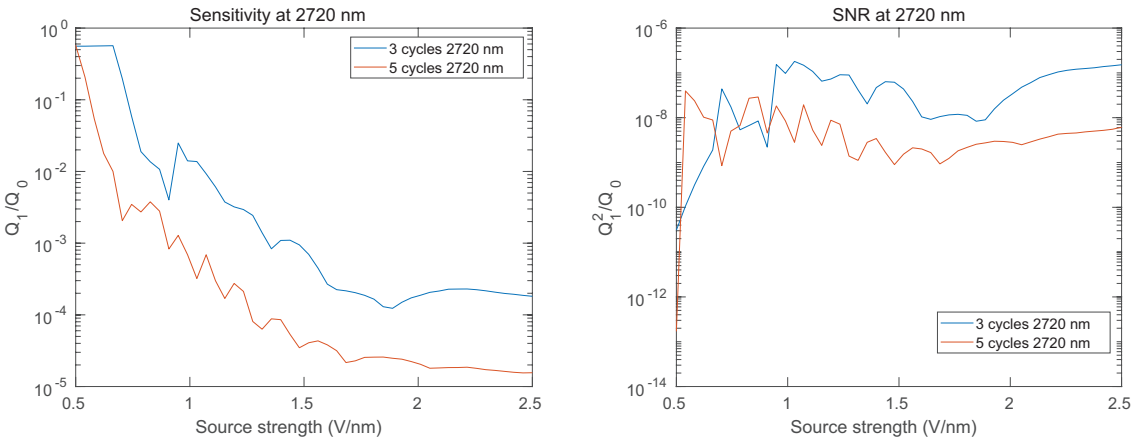

Figure 31: Sensitivity and SNR for thickness = 600 nm and length = 950 nm

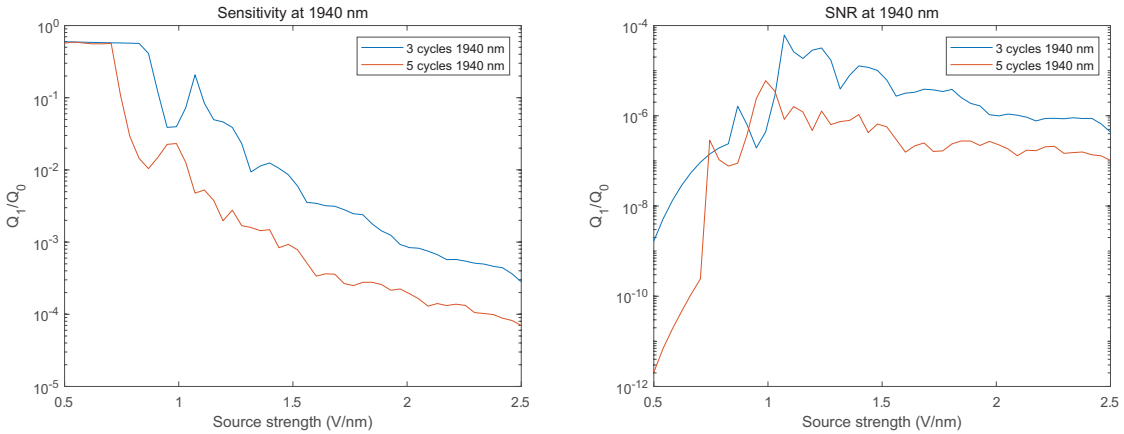

Figure 32: Sensitivity and SNR for thickness = 450 nm and length = 1000 nm

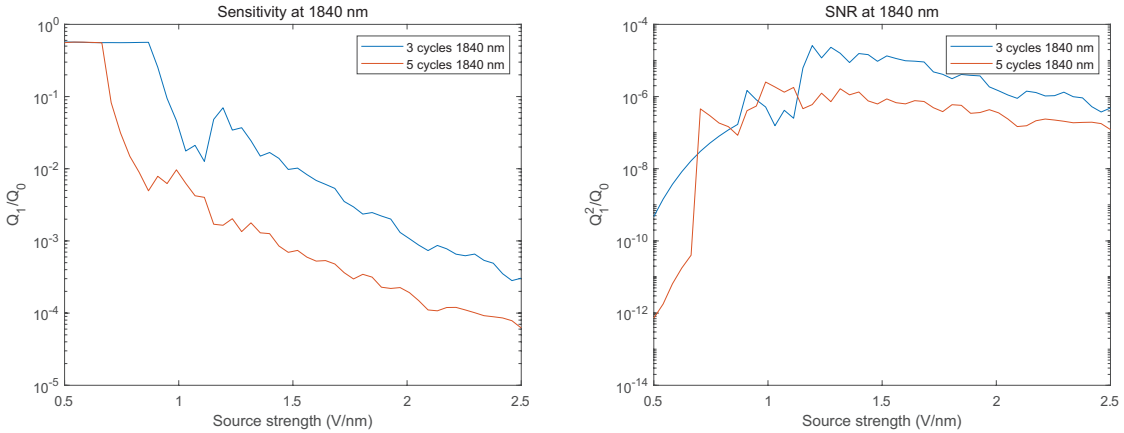

Figure 33: Sensitivity and SNR for thickness = 450 nm and length = 900 nm

- The CEP-sensitive photocurrent (Q1), defined as the difference between the peak value and the average of photoemission, does not follow the same trend. The value remains constant with the number of cycles but is shifted to a lower source strength value due to the higher optical emission. This observation also justifies the presence of a narrow region (source strength $< 1\,\mathrm{V\,nm^{-1}}$) where the SNR is favorable for the 5-cycle impinging radiation.

The presence of local minima in both the Sensitivity and SNR plots, corresponding to certain values of source strength, is related to the formation of *Vanishing points* [17]. This occurs due to the increase in envelope duration in the light/matter interaction. For specific source strength values, some sub-optical components emit photocurrent with the same magnitude but 180° out-of-phase. Consequently, there is a local reduction in the photoemitted component.

7.3 Triangular apex vs Teardrop apex

The final phase of the simulations is dedicated to comparing the device performance across different apex shapes.

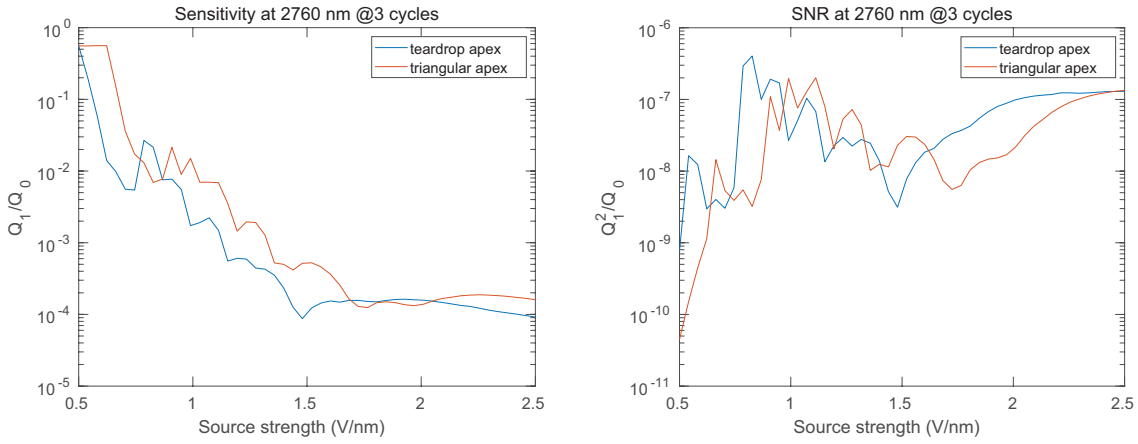

Figure 34: Apex comparison for thickness = 600 nm and length = 1000 nm

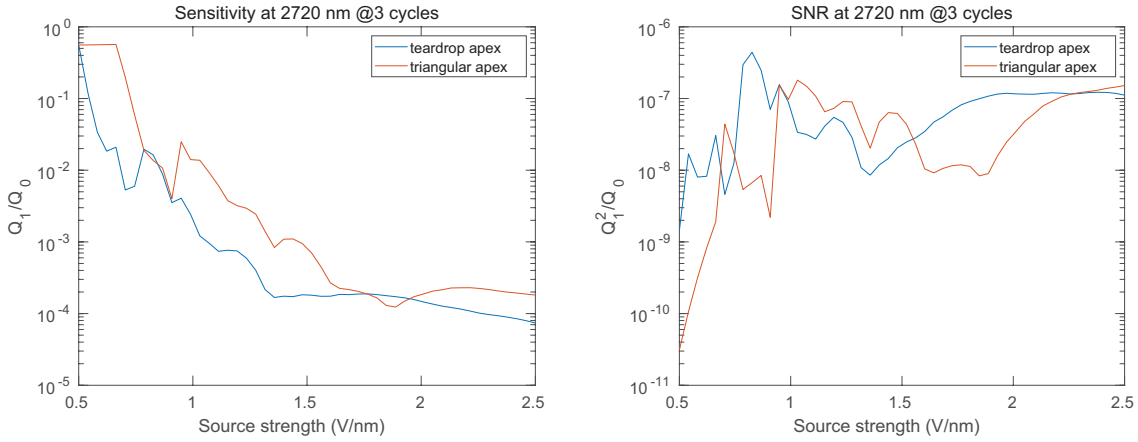

Figure 35: Apex comparison for thickness = 600 nm and length = 950 nm

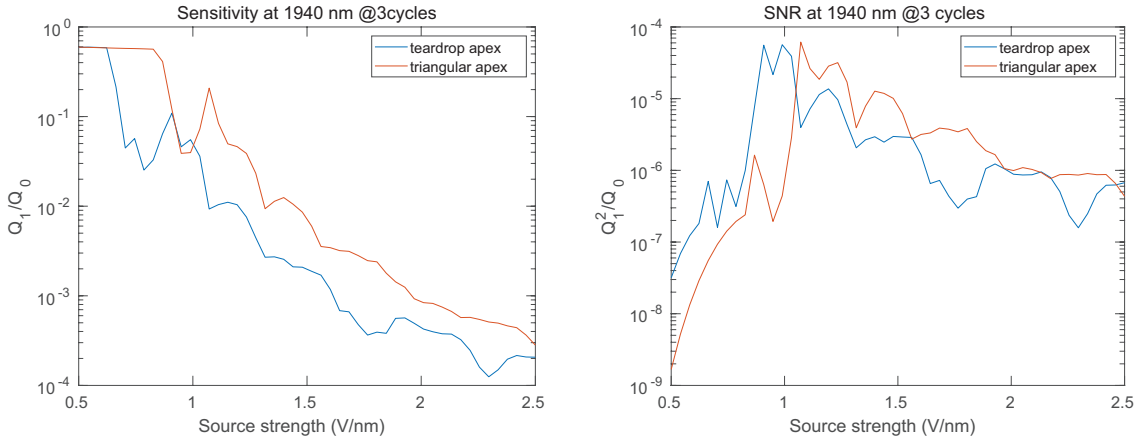

Figure 36: Apex comparison for thickness = 450 nm and length = 1000 nm

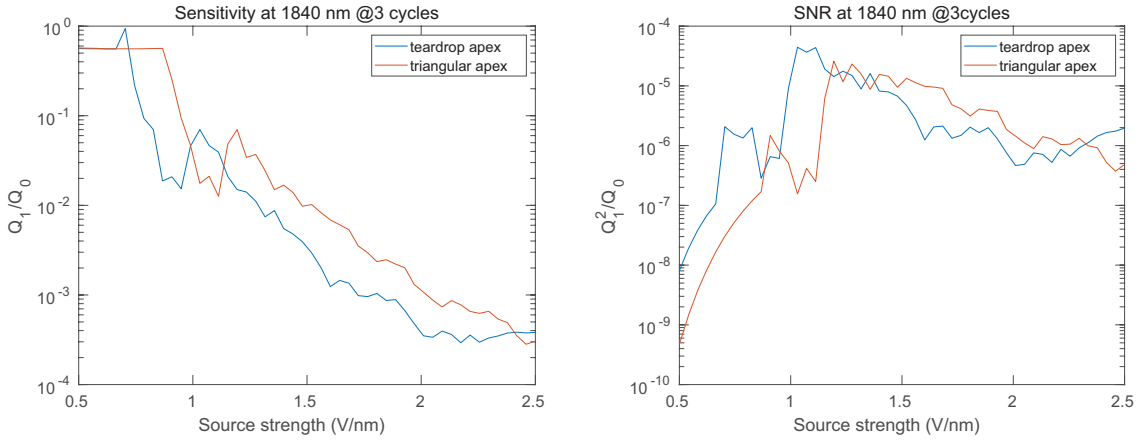

Figure 37: Apex comparison for thickness = 450 nm and length = 950 nm

As is evident from the comparison plot between the two apex shapes, the general trends for sensitivity and SNR remain consistent; however, they are shifted to lower source strength values for the teardrop case due to a higher field enhancement (FE). Specifically, the sensitivity follows a general downward trend with increasing source strength, except for a local maximum. On the other hand, the SNR exhibits an initial increase with source strength followed by a plateau. The prospect of attaining these two local maxima at lower source strengths (around $1\,\mathrm{V\,nm^{-1}}$ is particularly appealing in experimental settings where the laser source's power output has a limited range and cannot be elevated to high values to enter the optical emission regime.

8 Device Fabrication

The fabrication of the device was performed in MIT.nano, a cleanroom at the Massachusetts Institute of Technology. Considering the challenges related to the fabrication of the bow-tie configuration, in the first phase of this fabrication development both the asymmetric and the symmetric configurations are investigated.

8.1 SOI and Laser source

The technique and the steps of fabrication are mainly driven by the optical setup available in the laboratory. The fabricated device has to be compatible with the constraints related to the substrate and laser source.

We are interested in investigating both the optical and the electronic emission responses of the devices. Therefore, it is necessary to work with a conductive substrate of silicon. Silicon-on-insulator (SOI) chips are utilized in this study for two reasons:

- p-doped: substrates are commercially available.
- etch selectivity: high selectivity between silicon dioxide and silicon.

SOI pieces (30 mm × 30 mm), are diced from a 150 mm SOI wafer with a 220 nm thick silicon layer and oxide layer of 2 µm on a silicon carrier 675 µm.

The laser source available in the lab is based on Erbium-doped fiber:

- nonlinear polarization evolution-based (NPE) passive mode-locking is used to generate a 78.4 MHz pulse train (details can be found in [18]).
- The pulse is amplified and spectrally broadened using a highly nonlinear fiber. As the pulse propagates through the fiber, self-phase modulation takes place and a soliton is formed. Eventually, a higher-order soliton is formed which is nearly transform-limited. A prism pair is used to spatially filter out the higher-order soliton to be used in the experimental measurement. The central wavelength is 1200 nm and is 12 fs.

Several simulations have been run on COMSOL Multiphysics® to match the requirement of thickness and central peak wavelength. A FE spectra, design with thickness = 220 nm and rectangle length = 700 nm, is shown in [Fig. 38]. In this phase, it was necessary to find the correct recipe for each step of the fabrication process. Therefore, only the triangular apex shape has been investigated.

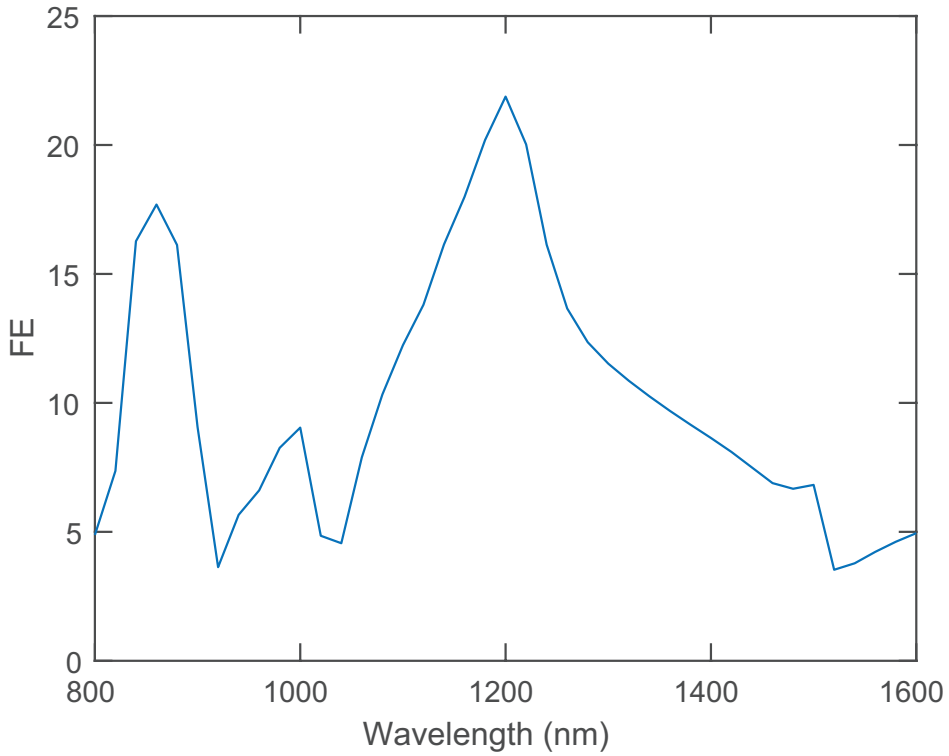

Figure 38: Simulated FE at the apex silicon/air interface for the fabricated device

Accordingly to what is discussed in Chapter [6.3], the transmission wires are centered in the region in which the nodes are formed. A suitable Python code, based on the PHIDL library, is used to generate the GDS layout [Fig. 39]. To the already developed code used in previous works, two features have been included:

- rectangle shape added to the triangular apex to obtain the cavity modes.
- transmission wire offset to match the correct position to avoid FE spectra

The targeted gap of 20 nm is the most challenging feature to realize in the fabrication step. A dose optimization of the electron beam lithography (EBL) step is necessary to achieve the 20 nm gap size. In order to avoid the nanoantenna apex shortage, a nominal gap sweep (from 20 nm to 70 nm) is performed. The idea behind this analysis is to reach the targeted gap even in design with higher nominal values because the beam spot size is approaching the targeted resolution.

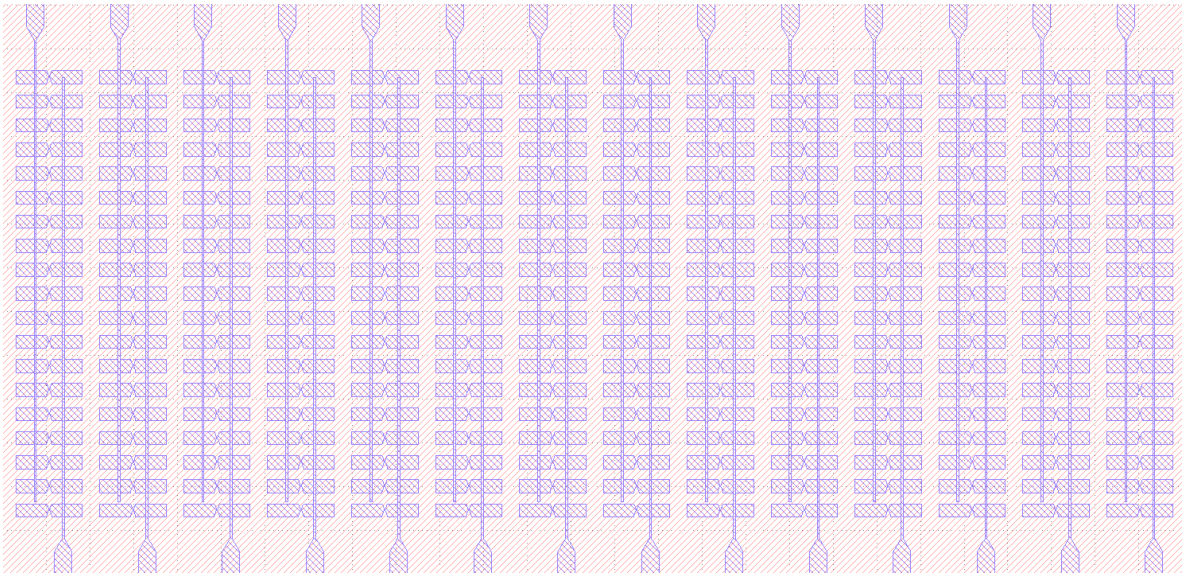

(a) symmetric array

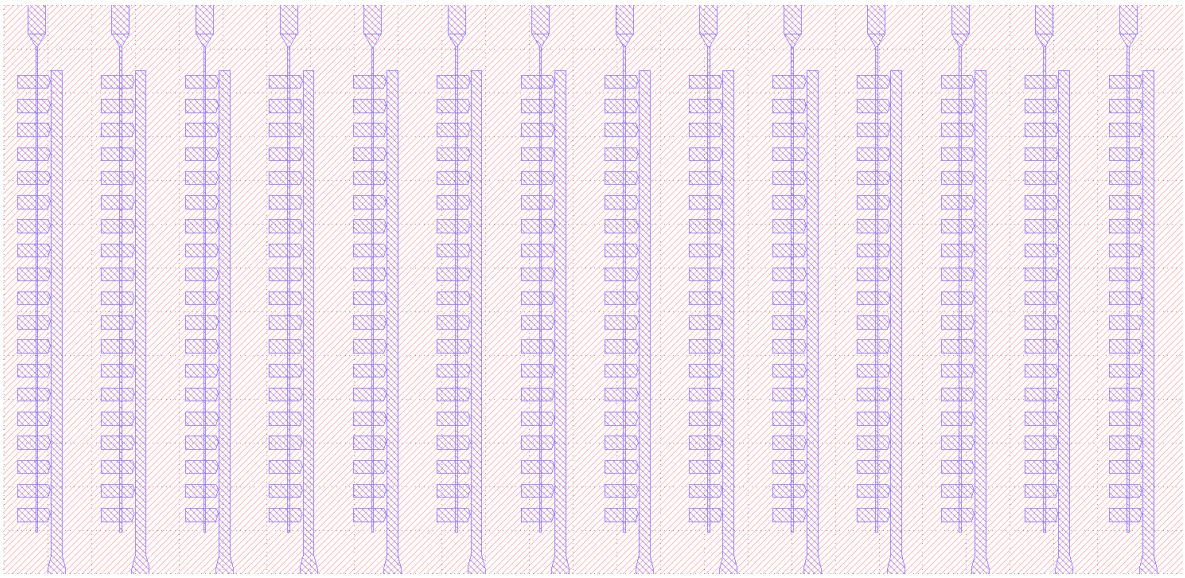

(b) asymmetric array

Figure 39: Symmetric and Asymmetric GDS arrays

Two different approaches are investigated in this work: the first one is based on the use of hydrogen silsesquioxane (HSQ) as a negative tone resist, and the second one is based on the hard mask technique.

8.2 HSQ

HSQ is an inorganic compound that behaves, after electron exposure, as a low-k Si oxide. This crosslinking-based process leads to a high selectivity for chlorine-based etching between the mask and silicon. It has also been demonstrated numerous times for sub-10 nm lithography.

Differently from other EBL resists, HSQ need to be stored at low temperature: shelf life is around 6 months when stored at $-5\,^{\circ}\mathrm{C}$ and around 9 months when stored at $-25\,^{\circ}\mathrm{C}$.

In the following subsection the fab process is detailed (starting with step 6, the described fabrication regards the contact pads and not the designed device):

1. CLEANING of the substrate: sonication on acetone bath for 60 sec and rinse with Isopropyl alcohol (IPA).

2. SPINNING of the HSQ: The surface of the chip is covered in 4% resist that is dispensed through a pipette in the center of the squared SOI chip. The vacuum is applied to the holder to maintain the sample still during the rotation (3 kRPM for 60 sec) [Fig. 40.1]

3. LITHOGRAPHY with Elionix HS-50: The squared SOI chip is divided into 4 smaller squared regions to evaluate the effect of writing at the same dose with different e-gun currents. Indeed, from the relationship $DOSE \propto t \times I_0$, it is possible to reduce the exposure time using higher current, at the cost of a larger spot size and therefore lower resolution. The gun has been calibrated to expose 2 squares at 1 nA, 1 square at 2 nA and 1 square at 5 nA. Both the symmetric and the asymmetric configurations are designed with 6 different gap sizes, and all the 12 arrays are written with 4 different doses: (1800 1900 2000 2100) $\mu C\,cm^{-2}$.

4. DEVELOPMENT: The exposed HSQ is developed in 25% tetramethylammonium Hydroxide for 60 sec. Then, the chip is rinsed in water. A silicon oxide mask with the desired pattern is now present on top of the silicon layer [Fig. 40.2].

5. ETCHING with RIE-Mixed-SAMCO-230iP: An RF signal is applied to generate the plasma end to selectively remove the silicon. Chlorine gas is introduced in the plasma chamber to obtain an anisotropic etch profile (an aspect ratio of around 11 is targeted). The etching step has been performed for 90 sec. Finally, ellipsometry was performed to verify that all the silicon was removed and the buried oxide exposed [Fig. 40.3].

6. OXIDE MASK ETCHING: The oxide mask is finally removed through buffered oxide etch (BOE) 7:1 (HF: NH4F = 12.5: 87.5%) for 90 sec [Fig. 40.4].

7. SPINNING: nLOF2035 (negative resist) has been spun at 3 kRPM for 60 sec. Due to its high thermal stability, this resist is suitable especially for the lift-off process.

8. PRE-EXPOSURE BAKE: A thermal step (110 °C for 90 sec) is necessary to evaporate the solvent and therefore obtain a solid film.

9. LITHOGRAPHY with Heidelberg Maskless Aligner MLA150: The contact pad design has no challenging features to be reproduced (tool resolution near 1.5 µm), therefore a free beam laser can be used to expose the resist with a dose of $300\,mJ\,cm^{-2}$ at a wavelength of 375 nm. Marks, previously patterned with EBL, are used to correctly align the pads with the already fabricated device.

10. POST-EXPOSURE BAKE: A thermal step (110 °C for 90 sec) is performed to reduce the standing wave effect.

11. DEVELOPMENT: AZ726 (2.38% TMAH in H_2O) is used to develop the unexposed area.

12. DEPOSITION with Temescal FC2000: 20 nm of gold and 2 nm of titanium (for adhesion) are deposited through metal evaporation. An electron beam heats the target under a high vacuum (10^{-6} Torr), and the evaporated atoms of the metal precipitate onto the substrate to form a film.

13. LIFT-OFF: The chip is put into an NMP bath at 65 °C for 1 h. Because of the low thickness of the resist, the use of this organic solvent is sufficient.

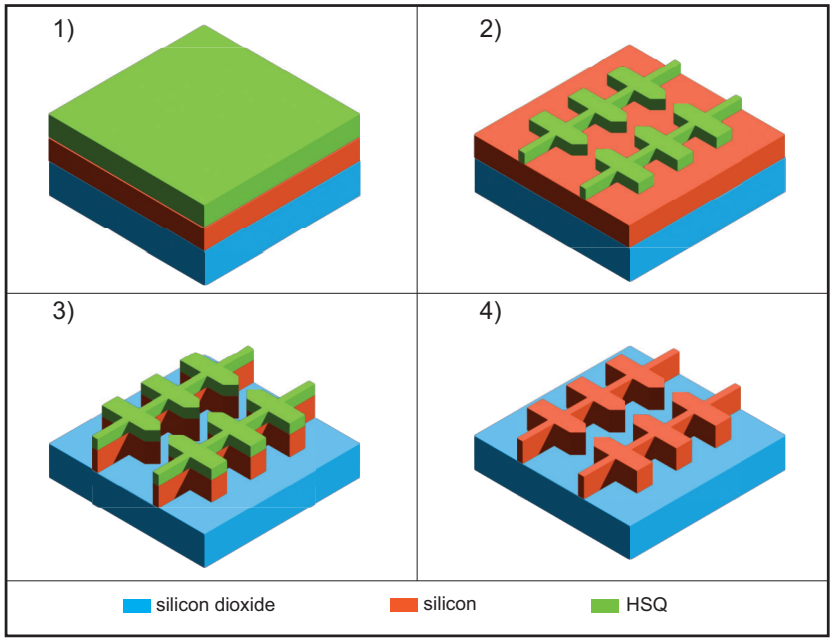

Figure 40: Device fabrication using HSQ

The nanoantenna arrays fabricated with an electron beam lithography tool operating at 1 nA are the ones that reproduce the GDS design with more fidelity. Nanoantennas exposed using higher current (2 nA and 5 nA) show rounded edges in the rectangular base and height directions.

1 nA-devices are then deeply investigated using a scanning electron microscope (SEM). I evaluate the difference in the gap as a function of the nominal gap in the design and of the dose. In the range from 1800 µC cm^{-2} to 2100 µC cm^{-2}, the dose does not play a major role in the gap formation, devices fabricated from the same design show similar features with slightly better resolution for the lower doses. As can be seen by [Fig. 41] [Fig. 42] [Fig. 43] [Fig. 44], the gap in the fabricated devices is larger with respect to the nominal value of a value between 10 nm and 15 nm (shadowing in the figures is related to charging effect due to nonconductive SiO_2 substrate). This shift is observed in most of the devices and for all the gap sweeps.

The reasons behind this result can be related to an exposure spot of the beam near the resolution limit (for the used beam current), or to an improper development process after the exposure. Indeed, as reported by [19], during the development of the unexposed HSQ a TMAH-insoluble layer can form at the surface limiting the etching mask resolution. This siloxane-type structure, investigated by x-ray photoelectron spectroscopy (XPS) in the paper, comes from a condensation reaction that transforms the soluble Si-H bonds in the Si-O-Si cross-linked bonds. A two-step development process (based on TMAH and dilute HF) is proposed to alternate the unexposed HSQ development and the siloxane layer removal to correctly obtain the 20 nm targeted gap.

8.3 Hard Mask

The previously mentioned bow-tie arrays of gold [3] and doped titanium nitride [4] were fabricated through lift-off.

In the first case, the gold nanoantennas (together with a titanium layer to increase adhe-

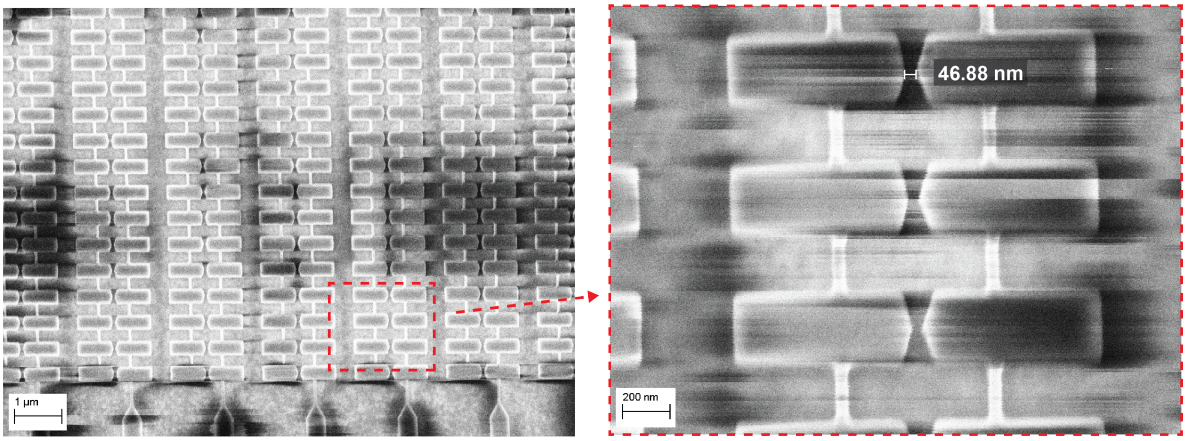

Figure 41: HSQ - Elionix HS-50, dose 1800 µC cm^{-2}, nominal gap 30 nm (after-etching)

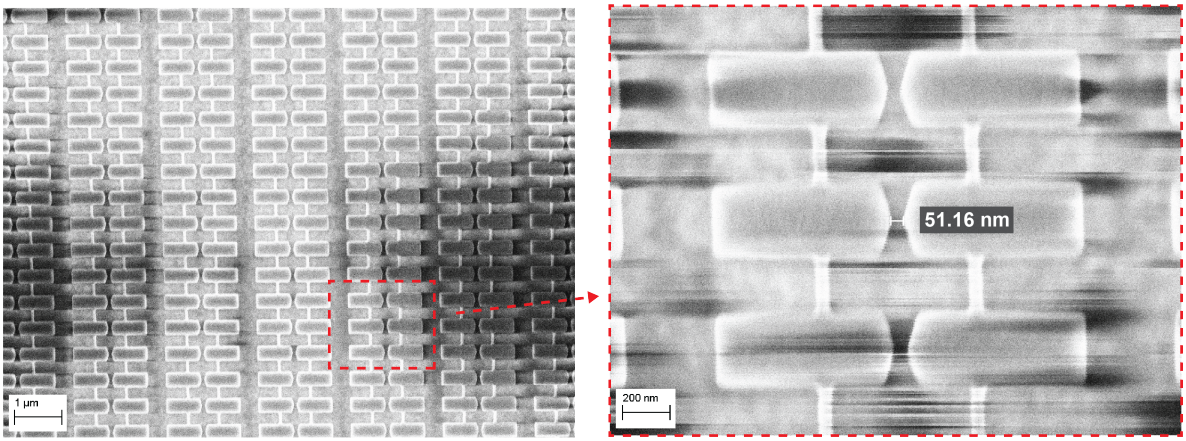

Figure 42: HSQ - Elionix HS-50, dose 1800 µC cm^{-2}, nominal gap 40 nm (after-etching)

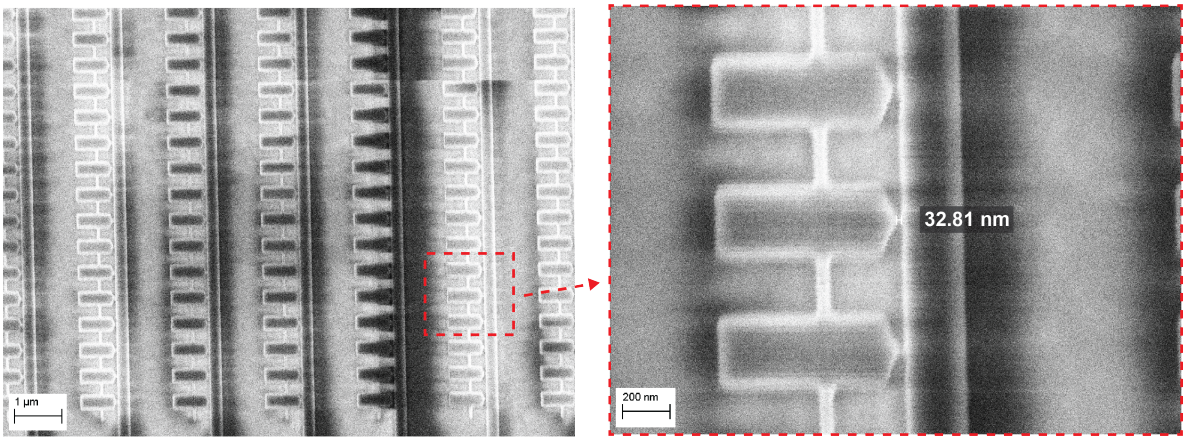

Figure 43: HSQ - Elionix HS-50, dose 1800 µC cm^{-2}, nominal gap 20 nm (after-etching)

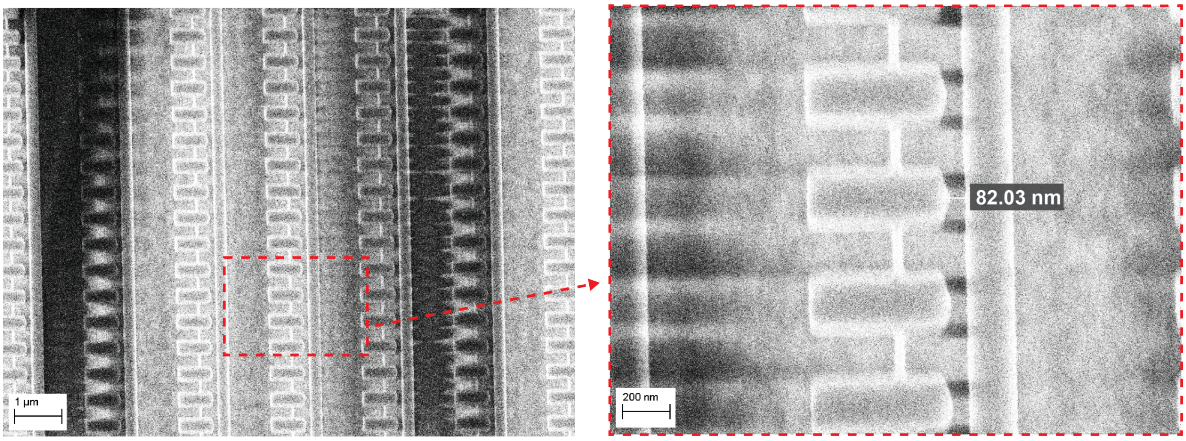

Figure 44: HSQ - Elionix HS-50, dose 1800 µC cm^{-2}, nominal gap 70 nm (after-etching)

sion) are directly realized through lift-off.

In the second case, instead, the lift-off process is performed to realize a bilayer Cr/Al hard mask and then etch the titanium nitride film through it. Masks made of just chromium and just aluminum have been also investigated: the first showed better performance but the following mask etching was not straightforward, the aluminum mask was instead easy to remove but the sidewalls were not perpendicular to the substrate (around 70° are fabricated. At the moment we are neither able to perform TMAH sonication to remove the bilayer mask nor to correctly etch the chromium. Therefore, aluminum is the mask material used in the following process (the contact pad steps are not listed [see above]):

1. CLEANING of the substrate: sonication on acetone bath for 60 sec and rinse with isopropyl alcohol (IPA).

2. SPINNING of the ZEP530A and PRE-EXPOSURE BAKE: The surface of the chip is covered in the positive resist (diluted 1:1 with anisole) that is dispensed through a pipette. The vacuum is applied to the holder to maintain the sample still during the rotation (3 kRPM for 60 sec). Heat treatment at 180 °C for 60 sec. ZEP530A differs from the widely used PMMA in a higher resistance to dry etch, instead their selectivity is similar [Fig. 45.1].

3. LITHOGRAPHY with Elionix HS-125: gap sweep from 20 nm to 70 nm with 10 nm spacing, dose sweep from 500 µC cm^{-2} to 650 µC cm^{-2} with 50 µC cm^{-2} spacing. The exposure current is set to 1 nA.

4. DEVELOPMENT: The unexposed positive resist is developed in o-Xylene for 30 sec. After that, the chip is rinsed with IPA for 30 sec. A silicon oxide mask with the desired pattern is now present on top of the silicon layer [Fig. 45.2].

5. DEPOSITION with Temescal FC2000: 20 nm of aluminum are deposited through metal evaporation. An electron beam heats the target under ultra-high vacuum, and the evaporated atoms of the metal precipitate into the substrate and form a film [Fig. 45.3].

6. LIFT-OFF: The chip is put into an NMP bath at 65 °C for 1 h. Therefore, the aluminum film above the resist is removed and only the hard mask remains on the silicon [Fig. 45.4].

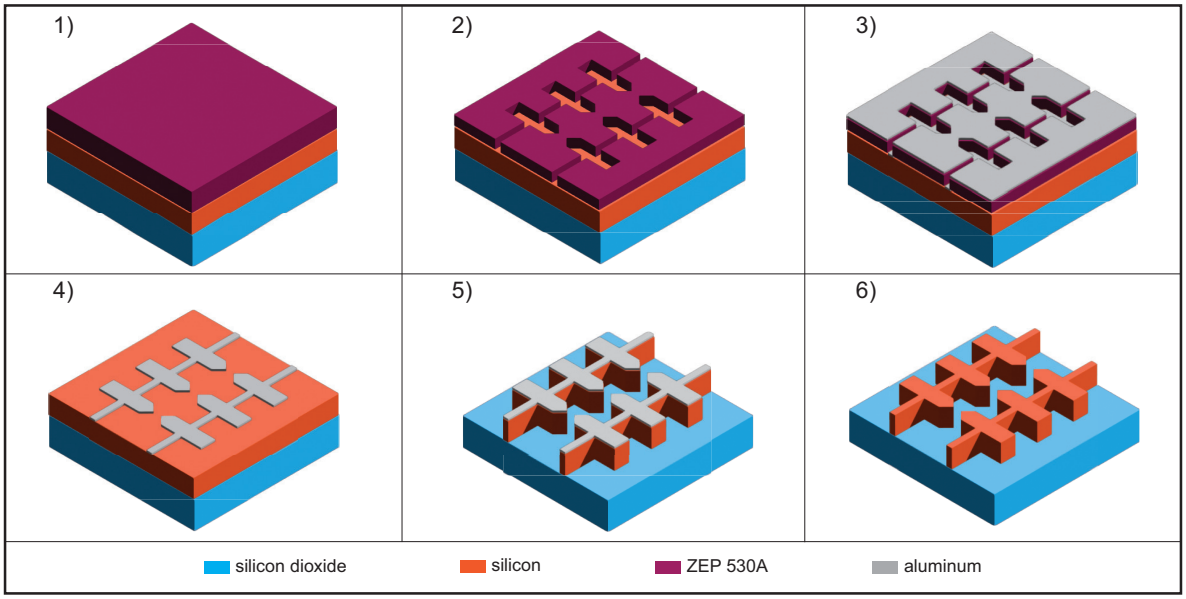

Figure 45: Device fabrication using Al hard mask

7. ETCHING with RIE-Mixed-SAMCO-230iP: An RF signal is applied to generate the plasma end to selectively remove the silicon. A chlorine-based etch is used to obtain an anisotropic etch profile (an aspect ratio of around 11 is targeted). The etching step was performed at 1 Pa for 90 sec with an ICP power of 150 W, bias of 100 W, and a Cl_2 flow rate of 15 sccm with 10 sccm of argon. Finally, an ellipsometer was used to verify that all the silicon was removed and the buried oxide exposed [Fig. 45.5].

8. ALUMINUM MASK ETCHING: The aluminum mask is finally removed through AZ726 (2.38% TMAH in H_2O) for 180 sec [Fig. 45.6].

The Al hard-masks shown in [Fig. 46], [Fig. 47], [Fig. 48], [Fig. 49] use different writing doses and nominally, the same gaps are all shorted. Even the 70 nm gap, which should be a safe feature size for EBL, is unable to be written. Both the gap and the side features of the nanoantennas look overexposed at the SEM. More precisely, the back of the nanoantennas on the left side is straight with sharp corners, the nanoantennas on the right, instead, have rounded edges. In this case, an error related to the beam spot size is not expected because of the asymmetric origin of the overdose problem. The mismatch with the GDS design, related to the direction of the electron beam displacement in the exposure phase, is more consistent with an erroneous calibration of the electron gun. The exposure of a test structure with different feature sizes and doses should be conducted to verify this hypothesis. In the alternative, reproducing a similar process with the different EBL tool (Elionix HS-50) can allow one to understand the origin of the problem.

8.4 Hetero-integration

Up to this point, both the simulations and the fabrication of the silicon nanoantennas have been carried out considering crystalline silicon. Exploring the possibility of realizing CEP-sensitive and optical field sampling devices in amorphous silicon (a-Si) can be interesting from the photonics hetero-integration point of view as it can be deposited on a variety of substrates either through plasma-enhanced chemical vapor deposition or physical vapor deposition (sputtering)

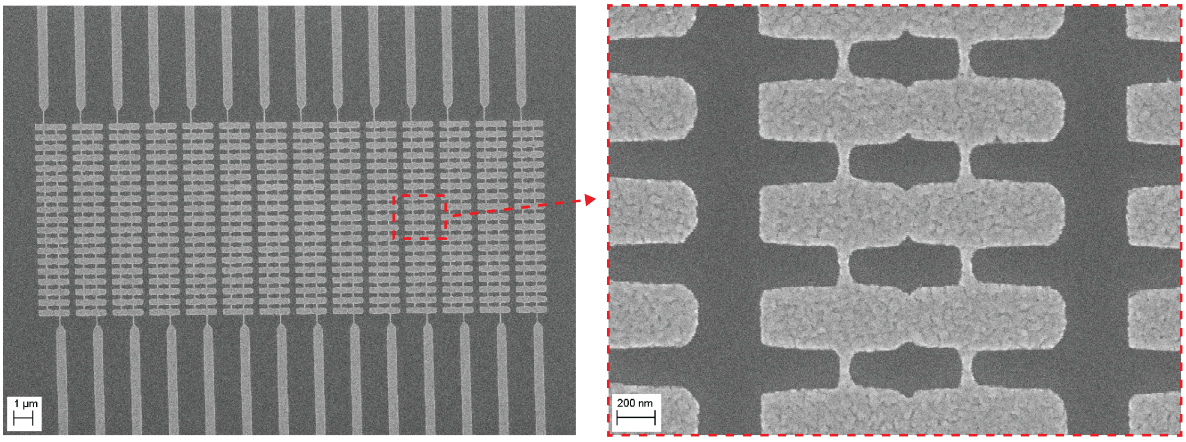

Figure 46: Al Hark Mask - Elionix FLS-125, dose 500 µC cm^{-2}, nominal gap 20 nm (pre-etching)

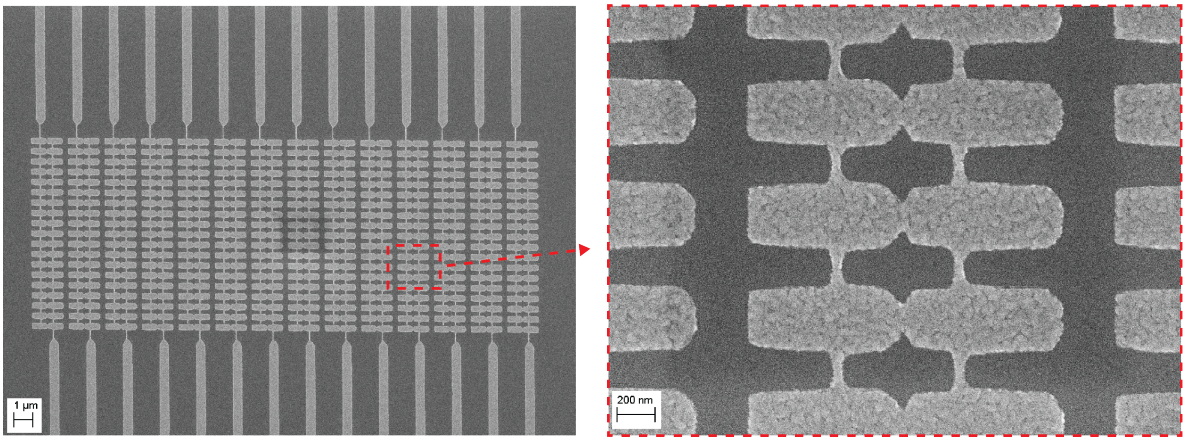

Figure 47: Al Hark Mask - Elionix FLS-125, dose 500 µC cm^{-2}, nominal gap 70 nm (pre-etching)

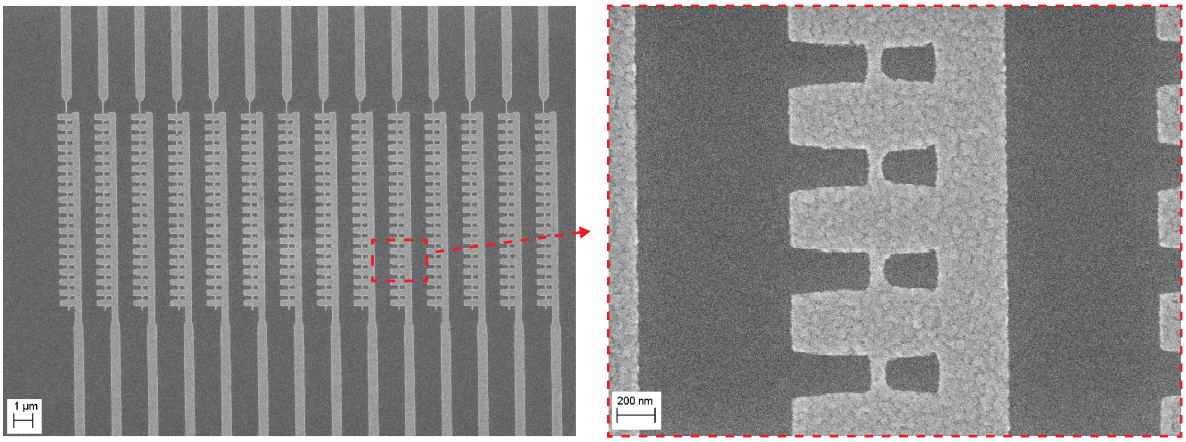

Figure 48: Al Hark Mask - Elionix FLS-125, dose 600 µC cm^{-2}, nominal gap 20 nm (pre-etching)

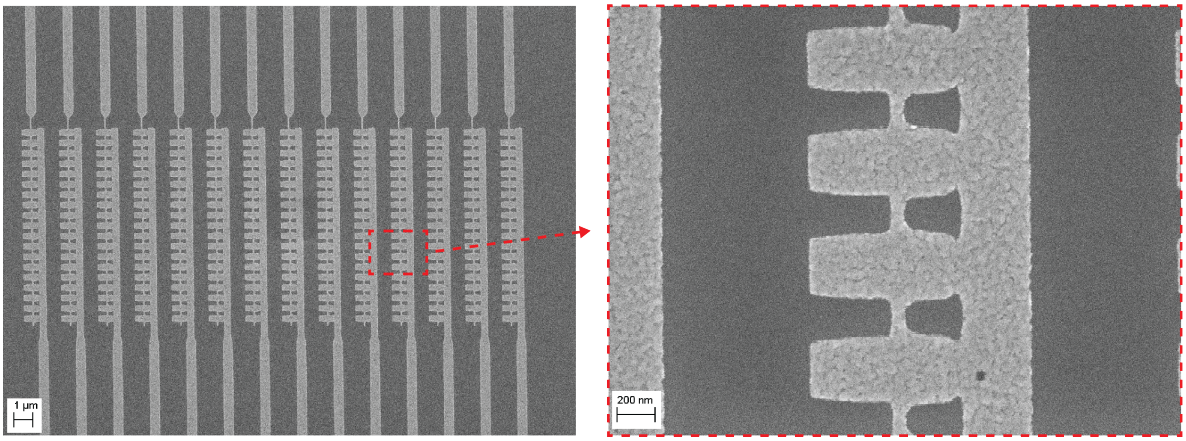

Figure 49: Al Hark Mask - Elionix FLS-125, dose 600 µC cm^{-2}, nominal gap 50 nm (pre-etching)

In plasma-enhanced chemical vapor deposition, a mixture of silane (SiH_4) and hydrogen (H_2) gases is introduced in a chamber to let the chemical species react and form an a-Si layer on the substrate. While in sputtering of undoped amorphous silicon, a plasma is generated into the reactive chamber, through the application of an RF signal, to bombard a silicon target with ions, which is physically deposited onto the substrate.

AJA ATC Orion series sputtering system is used to deposit the amorphous silicon on different substrates. a-Si films with varied thicknesses on sapphire and fused silica have been deposited. The thickness is controlled by changing the deposition time, then an ellipsometer is used to investigate the optical properties and film thickness after the sputtering of the a-Si. The value found through the interpolation of the thickness of various depositions is around 1.76 nm/min. This low deposition rate hinders the throughput of nanoantenna arrays designed with large thicknesses due to the instability of the argon plasma with time. However, with the slow deposition rate, I was able to realize 220 nm thick a-Si on sapphire or fused silica to target the 1200 nm resonance of the silicon nanoantenna array.

9 Conclusions and outlook

In this work, new designs for nanoscale structures that exploit dielectric materials to achieve large field enhancements ($FE > 10$), with broadband performance similar to plasmonic-based devices, have been presented.
In conclusion, Fabry-Perot-like resonant modes, if efficiently coupled with the apex, can be exploited to achieve a high local electric field at the silicon/air interface. While previous work on silicon-tip field-emitter arrays demonstrated similar field enhancements and operation in the optical-field emission regime[5], planar silicon devices supporting broadband field enhancements for optical field emission have yet to be considered before this work. This master's thesis presents:

- A new thin planar design for silicon nanostructures capable of exploiting broadband field enhancement with $FE > 10$ in dielectric structures thanks to low losses and high refractive index. Degradation and unreliability limits of previous nanoantenna designs should be mitigated through the use of such refractory devices.

- A study of the tunability properties of the resonant frequency through control of the thickness and rectangular length of the devices. It is possible to match the requirements of a broad range of ultrafast optical sources, from the visible to the near-infrared.

- A means to obtain further field enhancement through the use of a teardrop-shaped apex. The teardrop shape enhancess the coupling between the optical cavity mode and the apex, reaching higher FE ratios as in plasmonic devices. Thanks to this boost in field enhancement, it is possible to work at lower source strength without losing CEP sensitivity and SNR performance.

- Successful device fabrication which shows the possibility of heterogeneously integrating the silicon nanoantenna arrays on a wide range of integrated photonic and electronic platforms with a well-established and widespread fabrication process through the use of aSi. This is especially attractive for the future of femtosecond electronics. For example, previous work on nanostructures in the optical-field-driven tunneling emission regime shows how the generated electronic pulses can propagate in macroscopic striplines [2] across mm-scale distances on a chip surface. The possibility of replacing the plasmonic nanoantennas described in the article with a silicon-based device architecture would accelerate the widespread integration and adoption of femtosecond electronics.

However, some topics still require greater insight. The fabrication process needs optimization to achieve the target feature of 20 nm and to make a comparison with the results from simulations. Paying attention to the HSQ fabrication process, the investigation of the alternate unexposed resist development (TMAH and diluted HF) reported in Chapter 8 could facilitate the achievement of this goal.

Considering the limitations of any fabrication process, a more complete simulation study on FE metrics (central wavelength, bandwidth, and intensity of the peaks) as a function of small geometric parameter variations (e.g., 5% of the target value) will allow us to better understand the reliability of the entire fabrication process.

Additionally, investigating the capability of achieving considerable FE in the mid-infrared range and characterizing the optical properties (refractive index and extinction coefficient) of the a-Si films will be interesting for optimizing the nanoantenna design.

Some preliminary results from optical characterization, obtained using the laser source described in Chapter 8, suggest the possibility of optical-field-driven tunneling emission, but unfortunately the data remains unconclusive. Further testing will be warranted to fully

characterize the devices and understand their performance relative to the electromagnetic and optical-field-driven tunneling simulations presented in this work..

The fabricated arrays respond to incident illumination with an output current linearly dependent on the optical intensity of the laser pulses. We exclude a linear absorption mechanism (to overcome the potential barrier fixed by silicon electron affinity gap $\approx 4.01\,\mathrm{eV}$, silicon would need to absorb a photon with a wavelength $\approx 309\,\mathrm{nm}$, which is not present in the supercontinuum generated in the optical setup) We note that while the linear energy dependence is not expected through a pure FN tunneling model, prior experimental work from Si nanopillars has been shown to exhibit a linear and even sub-linear response [5]. There it was discussed that this is due to the electrons arising from a single ground state level which could be explained by electronic structure near the surface of silicon which could differ greatly from a metal like Au. In that case, the WKB tunneling rate from a single ground state might present a better fit to the experimental data and would explain the linear dependence with pulse energy that we observe. Furthermore, for certain nanoantenna arrays, the current drops by up to 33% when the linear polarization of the incident pulse train is rotated. This polarization dependence is consistent with optical-field-driven tunneling which is promising, but could also be explained by other factors such as polarization-dependent absorption warranting further analysis. Despite these remaining questions, I am confident thatwith a properly fabricated silicon device, the optical-field-driven regime will be clearly observed in the near future.

References

[1] Mina R Bionta, Felix Ritzkowsky, Marco Turchetti, Yujia Yang, Dario Cattozzo Mor, William P Putnam, Franz X Kärtner, Karl K Berggren, and Phillip D Keathley. On-chip sampling of optical fields with attosecond resolution. Nature Photonics, 15(6):456–460, 2021.

[2] Christoph Karnetzky, Philipp Zimmermann, Christopher Trummer, Carolina Duque Sierra, Martin Wörle, Reinhard Kienberger, and Alexander Holleitner. Towards femtosecond on-chip electronics based on plasmonic hot electron nano-emitters. Nature communications, 9(1):2471, 2018.

[3] Yujia Yang, Marco Turchetti, Praful Vasireddy, William P Putnam, Oliver Karnbach, Alberto Nardi, Franz X Kärtner, Karl K Berggren, and Phillip D Keathley. Light phase detection with on-chip petahertz electronic networks. Nature communications, 11(1):3407, 2020.

[4] A Nardi, M Turchetti, WA Britton, Y Chen, Y Yang, L Dal Negro, KK Berggren, and Phillip D Keathley. Nanoscale refractory doped titanium nitride field emitters. Nanotechnology, 32(31):315208, 2021.

[5] Michael E Swanwick, Phillip D Keathley, Arya Fallahi, Peter R Krogen, Guillaume Laurent, Jeffrey Moses, Franz X Kärtner, and Luis F Velásquez-García. Nanostructured ultrafast silicon-tip optical field-emitter arrays. Nano letters, 14(9):5035–5043, 2014.

[6] P. B. Corkum and Ferenc Krausz. Attosecond science. Nature Physics, 3(6):381–387, June 2007.

[7] Tara Fortier and Esther Baumann. Author Correction: 20 years of developments in optical frequency comb technology and applications. Communications Physics, 3(1):85, May 2020.

[8] Lu Chen, Wenqi Zhu, Pengcheng Huo, Junyeob Song, Henri J. Lezec, Ting Xu, and Amit Agrawal. Synthesizing ultrafast optical pulses with arbitrary spatiotemporal control. Science Advances, 8(43):eabq8314, October 2022.

[9] Margherita Maiuri, Marco Garavelli, and Giulio Cerullo. Ultrafast Spectroscopy: State of the Art and Open Challenges. Journal of the American Chemical Society, 142(1):3–15, January 2020.

[10] Felix Ritzkowsky, Mina R. Bionta, Marco Turchetti, Karl K. Berggren, Franz X. Kärtner, and Philip D. Keathley. Engineering the frequency response of petahertz-electronic nanoantenna field-sampling devices. In Conference on Lasers and Electro-Optics, page JW3A.56. Optica Publishing Group, 2022.

[11] Mena N. Gadalla, Andrew S. Greenspon, Michele Tamagnone, Federico Capasso, and Evelyn L. Hu. Excitation of Strong Localized Surface Plasmon Resonances in Highly Metallic Titanium Nitride Nano-Antennas for Stable Performance at Elevated Temperatures. ACS Applied Nano Materials, 2(6):3444–3452, June 2019.

[12] Andrew C. Strikwerda, Maksim Zalkovskij, Krzysztof Iwaszczuk, Dennis Lund Lorenzen, and Peter Uhd Jepsen. Permanently reconfigured metamaterials due to terahertz induced mass transfer of gold. Opt. Express, 23(9):11586–11599, May 2015.

[13] COMSOL Multiphysics®. Wave optics module, user's guide, 2018. https://doc.comsol.com/5.4/doc/com.comsol.help.woptics/WaveOpticsModuleUsersGuide.pdf.

[14] Mhd Marouf. Study of the damage threshold of optical surfaces of high-power energy pulse lasers with changing coefficient of optical surface roughness, and the damage threshold is increased by thermal treatment of optical glass. Journal of Physics & Optics Sciences, 01 2021.

[15] G Vuye, S Fisson, V Nguyen Van, Y Wang, J Rivory, and F Abeles. Temperature dependence of the dielectric function of silicon using in situ spectroscopic ellipsometry. Thin Solid Films, 233(1-2):166–170, 1993.

[16] Drew Buckley, Yujia Yang, Yugu Yang-Keathley, Karl K Berggren, and Phillip D Keathley. Nanoantenna design for enhanced carrier–envelope-phase sensitivity. JOSA B, 38(9):C11–C21, 2021.

[17] P. D. Keathley, W. P. Putnam, P. Vasireddy, R. G. Hobbs, Y. Yang, K. K. Berggren, and F. X. Kärtner. Vanishing carrier-envelope-phase-sensitive response in optical-field photoemission from plasmonic nanoantennas. Nature Physics, 15(11):1128–1133, November 2019.

[18] William P. Putnam, Phillip D. Keathley, Jonathan A. Cox, Andreas Liehl, Alfred Leitenstorfer, and Franz X. Kärtner. Few-cycle, carrier–envelope-phase-stable laser pulses from a compact supercontinuum source. J. Opt. Soc. Am. B, 36(2):A93–A97, Feb 2019.

[19] Hyo-Sung Lee, Jung-Sub Wi, Sung-Wook Nam, Hyun-Mi Kim, and Ki-Bum Kim. Two-step resist-development process of hydrogen silsesquioxane for high-density electron-beam nanopatterning. Journal of Vacuum Science & Technology B: Microelectronics and Nanometer Structures Processing, Measurement, and Phenomena, 27(1):188–192, 02 2009.